Novel erosion law based on CFD-DEM simulations and its application in hydromechanical modeling of gap-graded soils

Chuang ZHOU[a,b], Jiangu QIAN[a] , Zhen-Yu YIN[b*], Jie YANG[c]

Affiliations

[a] Department of Geotechnical Engineering, College of Civil Engineering, Tongji University, Shanghai 200092, China

[b] Department of Civil and Environmental Engineering, The Hong Kong Polytechnic University, Hung Hom, Kowloon, Hong Kong 999077, China

[c] College of Civil and Transportation Engineering, Shenzhen University, Shenzhen 518060, China

*Corresponding author: Dr. Zhen-Yu Yin, Tel:+852 3400 8470; Email: zhenyu.yin@polyu.edu.hk

Abstract: This paper develops a novel erosion law that incorporates the influence of stress state into the mass exchange between the liquid and solid phases for suffusion, using the coupled computational fluid dynamics and the discrete element method (CFD-DEM) simulations. To achieve this, a series of CFD-DEM simulation tests are conducted on gap-graded soil samples, followed by the derivation of a new erosion law that considers the influence of seepage velocity and mechanical conditions. The proposed erosion law is then integrated into a four-constituent framework to enable hydromechanical modeling. Furthermore, a fines-dependent constitutive model based on the critical state concept is implemented to account for the influence of suffusion on the mechanical behavior of the soil. The new model is assessed through a series of laboratory hydromechanical tests, yielding satisfactory estimation results. Subsequently, the model is utilized to investigate the influence of soil initial state, including void ratio, friction angle, fine content, and size ratio, on the evolution of erosion. Finally, the mechanical behavior of soils before and after suffusion is modeled using the proposed framework. The results demonstrate that the CFD-DEM-based erosion law, as well as the hydromechanical model, effectively capture the main characteristics of soils subjected to suffusion.

Keywords: suffusion; CFD-DEM; hydromechanical modeling; erosion law; gap-graded soil

1 Introduction

Suffusion refers to the migration and transportation of fine particles through the void matrix formed by coarse particles in gap-graded or internally unstable soils, driven by the seepage of water (Bendahmane et al. 2008, Wan and Fell 2008, Fell and Fry 2013). This phenomenon leads to a redistribution of the soil's pore structure, which significantly impacts both hydraulic and mechanical behavior, thereby influencing soil stability, leading to natural hazards. The occurrence of suffusion has also been linked to numerous damages and failures observed in hydraulic earth structures, making it an area of great academic interest (Xiong et al. 2020, Qian et al. 2021, Wang et al. 2022a, Zhou et al. 2023b). However, achieving a comprehensive understanding of suffusion poses significant challenges due to its involvement of multiple phases (solid soils and liquid water) and fields (hydraulic and mechanical). To address this, the development of a solid-liquid-hydro-mechanical model for suffusion is crucial. Such a model would enable a thorough comprehension of suffusion, facilitating its mitigation and prevention (Chen et al. 2021).

With the aid of advanced numerical techniques, the coupled Computational Fluid Dynamics (CFD) and Discrete Element Method (DEM) have emerged as prominent approaches extensively employed in suffusion research (Hu et al. 2019, Liu et al. 2020, Xiong et al. 2021, Wang et al. 2022a). This coupled method allows for the consideration of discrete characteristics inherent to sandy soils while explicitly accounting for solid-liquid interactions through interphase forces. Moreover, DEM serves as a powerful tool for tracking individual particles, providing insights into the microscopic interparticle contact forces that pose challenges in

53 experimental quantification. For instance, Zhou et al. (Zhou et al. 2022, 2023b) employed
54 CFD-DEM to construct a comprehensive set of Representative Volume Element (RVE) samples.
55 Through systematic analysis, they investigated the impact of particle morphology and cyclic
56 loading on the progressive development of suffusion. While the CFD-DEM approach has made
57 significant advancements, it is important to note that existing studies have primarily focused
58 on small-scale specimens due to the high computational demands involved. Striking a balance
59 between the number of particles and fluid mesh size is crucial to ensure computational
60 feasibility, which may result in certain discrepancies from real-world conditions. For example,
61 in a validation test conducted by Liu et al. (Liu et al. 2021) using CFD-DEM, the simulated
62 results exhibited good agreement with experimental trends but displayed some discrepancies
63 in finer details, such as the critical hydraulic gradient. These discrepancies can be attributed to
64 simplifications in particle gradation, sample size, and simulation time within the numerical
65 model. To enable the study of suffusion in larger-scale scenarios, such as dams and tunnels,
66 researchers have developed the four-constituent model within a continuous medium framework
67 (de Boer 2000, Uzuoka and Borja 2012, Schaufler et al. 2013). This model conveniently
68 integrates with the finite element method for solving boundary value problems (BVP) (Yang et
69 al. 2020, Yin et al. 2020). In this approach, the loss of fine particles is accounted for through
70 solid and fluid mass exchange. The progression of suffusion is estimated by solving a series of
71 mass balance equations. However, to solve these governing equations, an erosion law that
72 describes the rate of mass exchange between different phases becomes necessary.
73 To date, considerable efforts have been dedicated to the development of appropriate

74 erosion laws (Azadbakht et al. 2020, Deng et al. 2023). Many of these laws are derived from
75 empirical formulas based on experimental observations (Sterpi 2003, Cividini et al. 2009,
76 Uzuoka et al. 2012, Khalil et al. 2013). For example, Sterpi (Sterpi 2003) established a
77 relationship between the eroded fines and the hydraulic gradient, as well as erosion time. Liang
78 (Liang et al. 2019) applied this model to their experiments and found satisfactory results for
79 specific cases. However, the model failed to provide accurate predictions for different hydraulic
80 conditions when using constant material parameters. Uzuoka et al.(Uzuoka et al. 2012)
81 considered soil porosity and fine content, proposing a relationship between erosion rate and
82 fluid velocity. Nonetheless, this erosion law still exhibits a significant limitation as it does not
83 account for the influence of soil stress state on suffusion. Both numerical and experimental
84 studies have revealed that the development of fine particle erosion is governed by the stress
85 state of the soil. Chang et al. (Chang and Zhang 2013a) and Zhou et al. (Zhou et al. 2022)
86 reported that deviatoric stress can induce fabric anisotropy, exacerbating particle loss.
87 Furthermore, Liu et al. (Liu et al. 2020) discovered that the mass loss of samples under different
88 confining pressures (mean stress) varies. Unfortunately, there is currently no erosion model
89 that adequately considers the influence of soil stress conditions, which poses a hindrance to
90 hydro-mechanical modeling of suffusion. It is worth noting that Deng et al (Deng et al. 2023)
91 recently proposed an erosion law that incorporates surcharge pressure, but the inclusion of
92 mean stress and deviatoric stress, which are commonly encountered in soil testing, has not yet
93 been addressed. Therefore, there is an urgent need for further research to develop a new erosion
94 law that encompasses the soil stress state.

This study aims to propose a novel erosion law that facilitates the hydro-mechanical modeling of suffusion within the framework of the four-phase continuum theory. Notably, the erosion law is derived from the results of CFD-DEM simulations rather than physical experiments. This is because, the numerical method is efficient and can pay less effort in labour, meanwhile it can achieve similar results to tests. In addition, it's more convenient for CFD-DEM to establish samples under different mean stress and the deviatoric stress, so that an erosion law that considers both the complex stress state, as well as the fluid velocity can be determined. The newly proposed model, as well as the hydro-mechanical framework is validated by a series of laboratory experiments, demonstrating good agreement and indicating their effectiveness in simulating suffusion in gap-graded soils.

2 CFD-DEM simulations and novel erosion law

The coupled CFD-DEM method is implemented through the integration of three modules, i.e., DEM, CFD, and the CFD-DEM coupling packages (Kloss et al. 2012). The DEM package is responsible for solving the governing equations of Newton's motion law, allowing for the determination of particle velocities, positions, and contact forces (Cundall and Strack 1979). On the other hand, the CFD package serves as the solver for the averaged Navier-Stokes equations, providing fluid pressure and velocity values for each discretized cell in an Eulerian manner. The interactions between the solid and fluid phases, such as drag forces and pressure gradient forces, are obtained through the coupling of the CFD and DEM codes. For the sake of simplicity, the respective governing equations (Zhao and Shan 2013, Hu et al. 2023) for the different packages are summarized in Appendix A.

2.1 Testing soils and schemes

The gap-graded soil used in this study is based on HK-CDG mixtures, consisting of decomposed granite and sand, as employed in previous experiments (Chang and Zhang 2013a, Xu et al. 2022). As is shown in Fig. 1, the fine content of HK-CDG is evaluated as 35%. The particle sizes range from 0.09 to 0.15 mm for the fine particles and from 1.5 to 5 mm for the coarse particles. To accommodate computational limitations, a narrower range of grain diameters is selected and utilized in the CFD-DEM simulations. Following the approach of Liu et al. (Liu et al. 2021), the simplified soil retains the same fine content, with a constant fine particle size of 0.2 mm and coarse particle size of 1.2 mm, resulting in a gap ratio (defined as the size ratio between coarse and fine particles) of 6. The numerical samples are represented as cuboids composed of ideal spherical particles. To compensate for the discrepancies caused by the shape simplification, a rolling resistance model is introduced (Ai et al. 2011, Wensrich and Katterfeld 2012). As shown in Fig. 2, the sample is enclosed by six rigid walls. During suffusion, the top wall is replaced by a filter with holes that only allows the passage of fine particles. The seepage direction is set as upward to eliminate the influence of downward gravity (Xiong et al. 2020, Zhou et al. 2023a). The CFD domain has a larger length than the DEM domain to ensure that all particles are covered by the fluid. Other key input parameters, such as friction coefficient, Young's modulus, and timestep, are referenced from similar studies (Qian et al. 2021, Wang et al. 2022b, Xiong et al. 2022), as listed in Table 1.

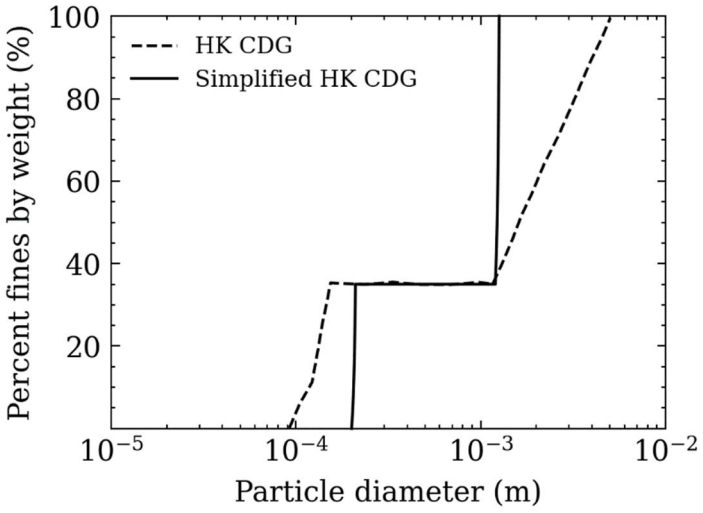

Fig. 1 Grain-size distribution of soils in this study and experiment

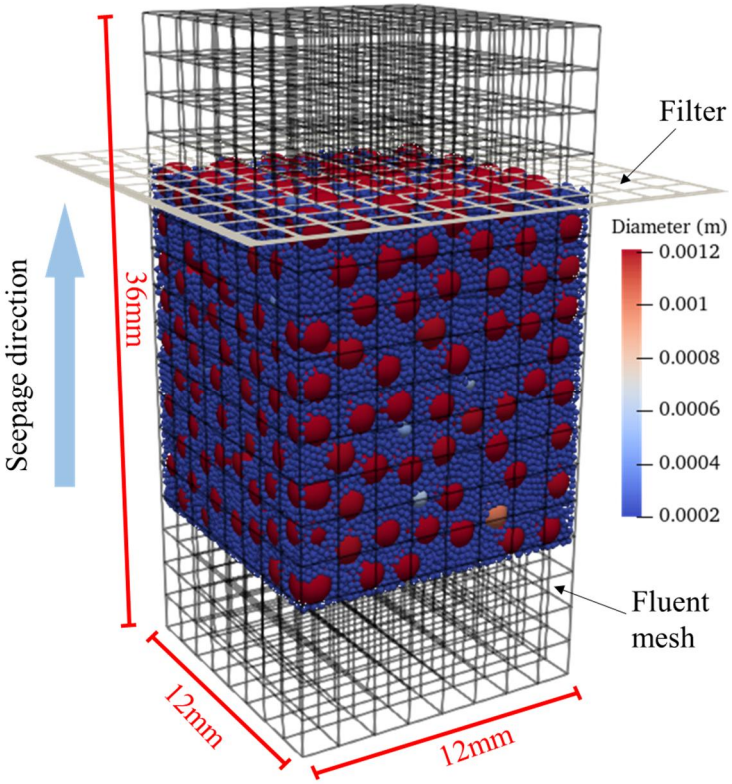

Fig. 2 Illustration of CFD-DEM model

143 Table. 1 Summary of model parameters

Model parameters		
DEM	Young's modules, E	5×10^{7}
	Poisson's ratio, μ	0.3
	Friction coefficient, μ_c	0.3
	Rolling friction coefficient, μ_r	0.1
	Time step (s)	2×10^{-7}
	Density, ρ_s (kg/m^3)	2.65×10^{3}
CFD	Fluid viscosity, ν (Pa·s)	1×10^{-3}
	Density, ρ_f (kg/m^3)	1×10^{3}
	Cells (mm)	$1.2\times1.2\times1.2$
	Time step (s)	2×10^{-3}

144

145 The objective of this study is to investigate the influence of seepage velocity, confining
146 pressure (mean stress) and stress ratio on solid-liquid mass exchange. To achieve this, a total
147 of 11 samples are established with varying hydraulic gradients ($i=2,3,4,6,8,12$m/m), mean
148 stresses ($p=50,100,150,200$kPa) and stress ratios ($\eta=q/p=0,0.3,0.5,0.75$, where q is
149 deviatoric stress) are established. The details of these samples are provided in Table. 2. The
150 simulation procedure involves initially compressing the samples to the predetermined pressure
151 using the wall. Subsequently, upward flow is induced by creating a pressure difference between
152 the inlet and outlet of the CFD domain. Throughout the suffusion process, the stress on the wall
153 remains constant. Fine particles are carried and migrate within the soil matrix, and once a
154 particle passes through the filter, it is removed from the simulation by the DEM domain to
155 simulate mass loss. The simulation time is determined based on the criterion that no further
156 loss of fines occurs. However, slight differences in simulation time may arise due to different
157 stress conditions, ranging from 8.5 to 12.5 seconds.

158

159 Table. 2 Summary of model parameters

No.	i (m/m)	p (kPa)	η (q/p)	Initial void ratio e_0	Initial hydraulic conductivity k_0 (cm/s)	Simulation time (s)
1	2	50	0	0.335	2.10×10^{-3}	8.5
2	3	50	0			8.5
3	4	50	0			8.5
4	8	50	0			8.5
5	12	50	0			8.5
6	4	100	0	0.332	2.11×10^{-3}	8.5
7	4	150	0	0.328	2.11×10^{-3}	8.5
8	4	200	0	0.326	2.16×10^{-3}	8.5
9	4	50	0.3	0.321	2.06×10^{-3}	8.5
10	4	50	0.5	0.325	2.05×10^{-3}	12
11	4	50	0.75	0.335	2.12×10^{-3}	12.5

160 **2.2 Results of the fines mass loss**

161 Fig. 3 shows the percentage of fines mass loss m_e, which is given by the ratio of the
162 cumulative lost mass and the initial fines mass. Generally, the evolution of mass loss shows an
163 initial high rate, followed by a decrease with increasing suffusion time, and eventually reaching
164 a steady state where the loss of fine particles becomes negligible. These numerical results align
165 well with observations from physical experiments (Marot et al. 2012, Chang and Zhang 2013b,
166 Ke and Takahashi 2014a). As the hydraulic gradient (seepage velocity) increases, the fluid
167 exerts a stronger drag force on fines, facilitating particle transportation and resulting in
168 increased fines loss. It is noteworthy that the relationship between the maximum mass loss ratio
169 and seepage velocity exhibits significant nonlinearity. Specifically, when the hydraulic gradient
170 is below 2m/m, the specimen does not exhibit visible fines loss. As the hydraulic gradient
171 increases to 3m/m, the mass loss slightly increases. However, when the hydraulic gradient is
172 increased from 3 to 4m/m, the mass loss significantly increases. Subsequently, when the
173 hydraulic gradient is increased from 4 to 12m/m, the increase in mass loss becomes very limited.

Laboratory experiments (Chang and Zhang 2013a) have also confirmed such nonlinear behavior. On the other hand, an increase in mean stress enhances particle connection, thereby increasing erosion resistance and decreasing mass loss. Conversely, the presence of deviatoric stress leads to an anisotropic distribution of contact forces, increasing the likelihood of particle migration and resulting in more fines loss (Zhou et al. 2022, Liu et al. 2023).

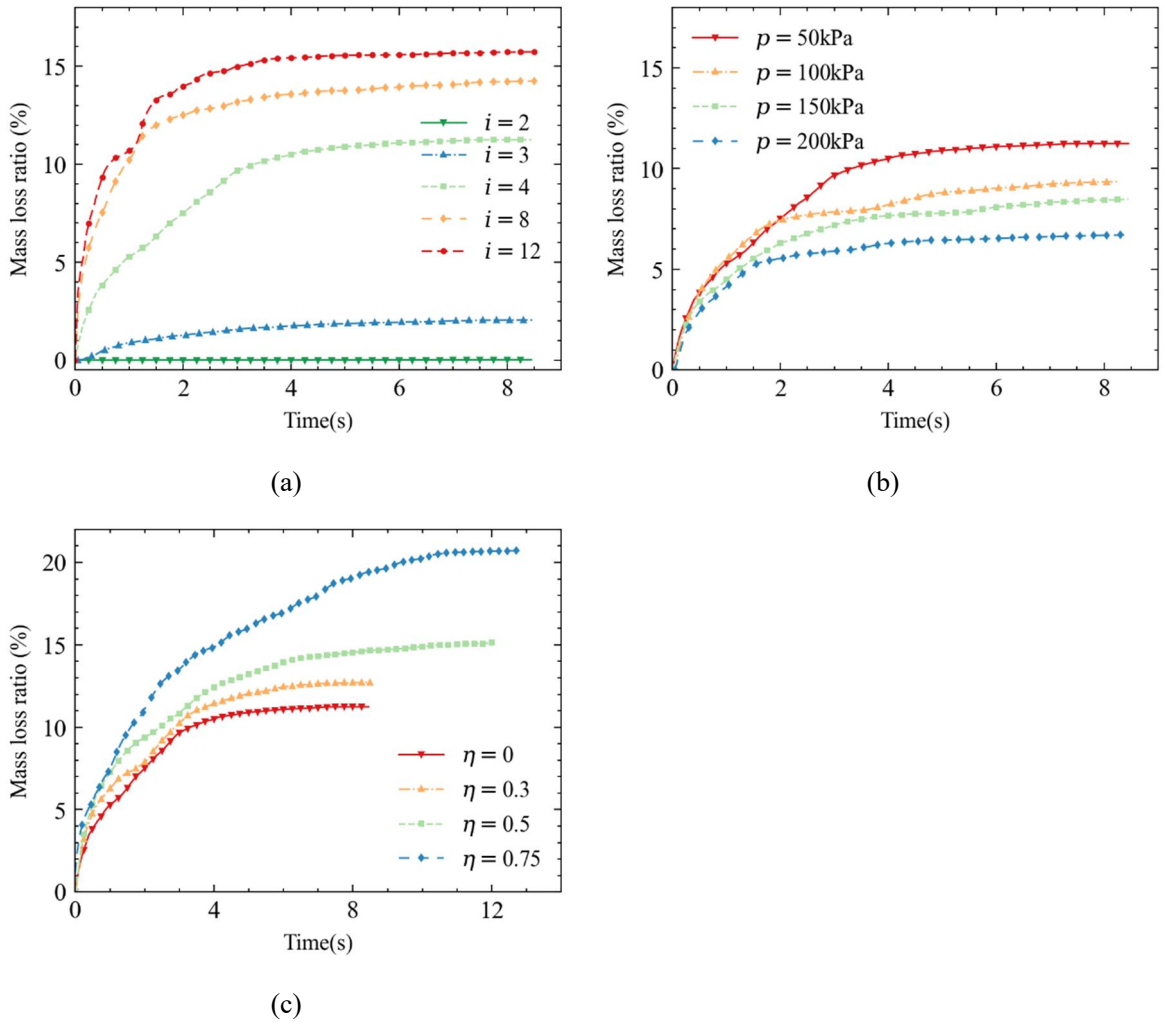

Fig. 3 Fine particle mass loss ratio for samples under different conditions: (a)confining pressure; (b) hydraulic gradient; (c) stress ratio

2.3 Novel erosion model

To derive the erosion law in the following section, which describes the rate of volumetric mass loss exchange from fine particles to the fluid, a cumulative mass equation is first

184 introduced. Based on the observations from Fig. 3, it is evident that the evolution of the mass
185 loss ratio follows the patterns of exponential functions. Therefore, the following exponential
186 formula is proposed:

$$m_e = m_\infty[1-\exp(-\lambda v_f^a (p/p_{ref})^b t)] \quad (1)$$

187 where m_e is the mass loss ratio, and v_f denotes the seepage velocity. p and p_{ref} are the
188 mean stress and reference stress, respectively. In this study, the p_{ref} is uniformly specified as
189 50kPa. t is the suffusion time. λ, a, b are soil-related material parameters. m_∞ is the
190 maximum mass loss ratio when seepage erosion stabilizes. It is a function of seepage velocity,
191 mean stress and stress ratio, given as:

$$m_\infty(v_f, p, \eta) = m_0 \frac{\exp(k_1 p/p_{ref} + k_2(\eta/M_p)^c)}{1+\exp(k_3(v_f - v_{fc}))} \quad (2)$$

192 where M_p is the soil peak stress ratio (according to the DEM triaxial results, the peak stress
193 ratio for HK-CDG is determined as 0.85 in this study), and v_{fc} is a critical seepage velocity.
194 m_0, k_1, k_2, k_3, c are fitting parameters. Eqn.(2) indicates that for a given confining pressure and
195 stress ratio, as the seepage velocity increases, m_∞ approaches m_0, and the mass loss does not
196 increase infinitely. This is because, based on the tests conducted, there is always a portion of
197 fines that remains in the soil regardless of the level of hydraulic gradient. All the unknown
198 parameters in Eqn.(3) can be calibrated by fitting the data of the ultimate mass loss ratio m_∞
199 under different test conditions. Fig. 4 presents the fitting results of Eqn.(2), and the calibrated
200 parameters are listed in Table.3. Once the Eqn (2) is determined, it can be substituted into Eqn
201 (1), allowing the unknown parameters in Eqn (1) to be calibrated using the time evolution curve
202 of the mass loss ratio obtained from CFD-DEM, as shown in Fig. 5. From the fitting curves in

Fig. 4 and Fig. 5, it can be found that the proposed mass loss ratio formula can well correspond to the results from CFD-DEM simualtions for most cases.

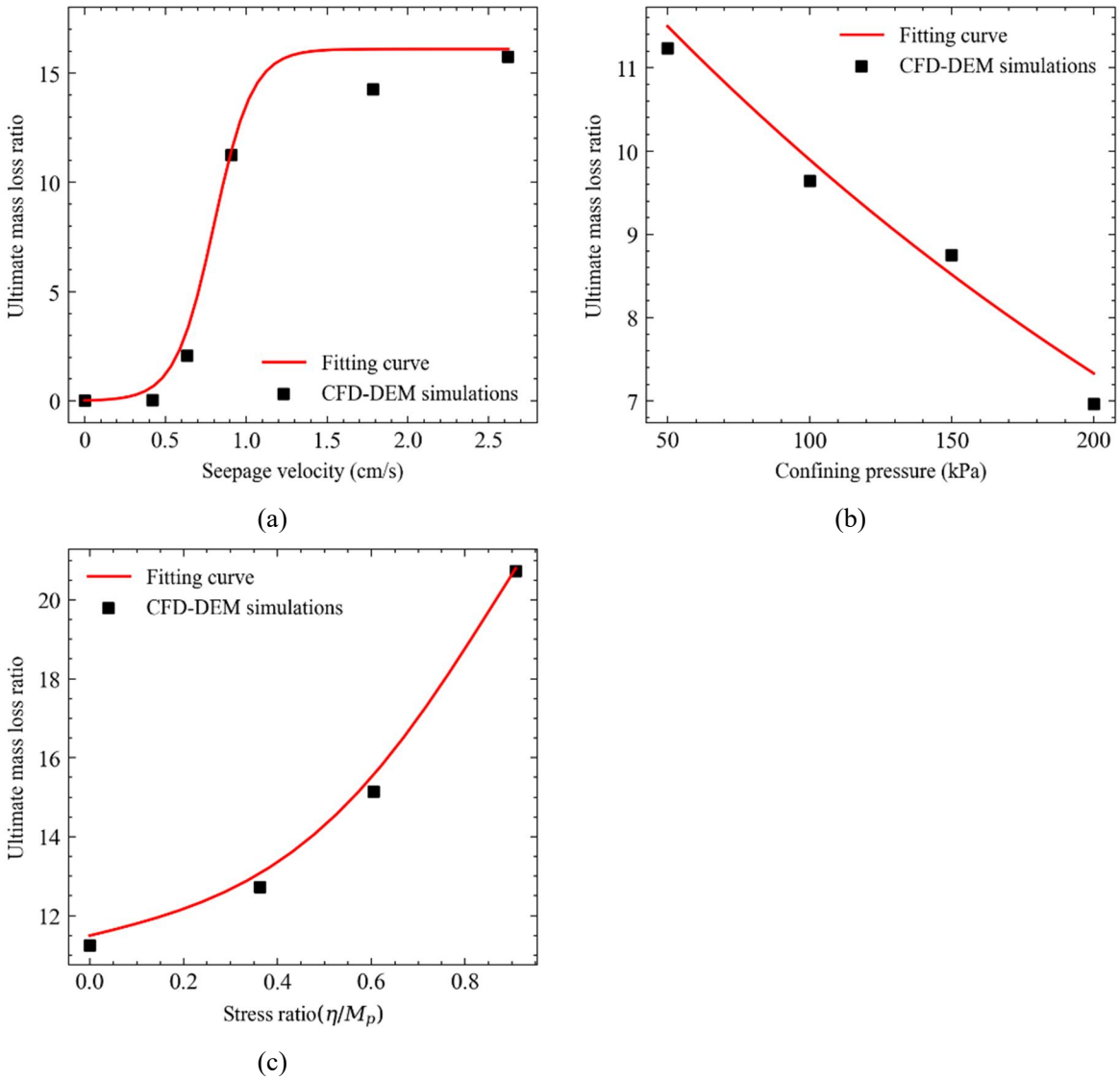

Fig. 4 The fitting curve of ultimate mass loss ratio for different: (a) seepage velocity; (b) confining pressure; (c) stress ratio

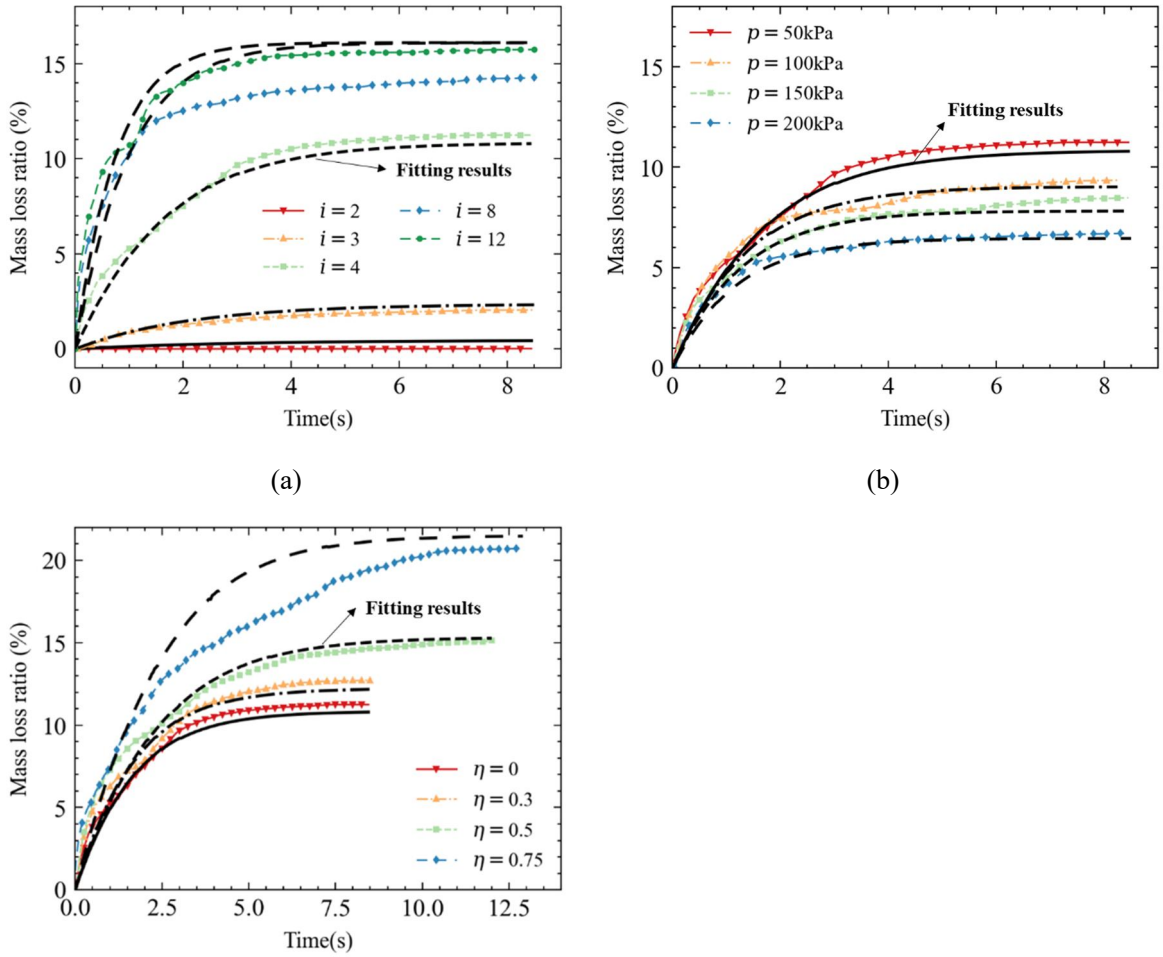

Fig. 5 Fitting results of mass loss ratio versus time for cases under different conditions: (a) seepage velocity; (b) confining pressure; (c) stress ratio

Table. 3 Parameters of the mass loss ratio model.

Soil	λ	a	b	c	m_0	k_1	k_2	k_3	v_{fc} (cm/s)	p_{ref} (kPa)
HK-CDG in this study	178.5	0.75	0.2	1	18.7	-0.15	0.4	8.3	0.8	50
Liang et al. (Liang et al. 2017)	32	1.5	-0.4	1	17	0.12	0.98	-20	0	20

To further validate the effectiveness of the model, the calculated results are compared with experiments conducted by Liang et al.(Liang et al. 2017) using gap-graded soils (as illustrated in Fig. 6). The mean stress and deviatoric stress in the experiments were applied using

confining and vertical loading systems, thus soil with different initial stress states could be obtained. Subsequently, the samples were subjected to an upward seepage flow through a water supply system. By adjusting the height of the upstream water tank, various hydraulic gradients could be imposed. For the purpose of validation, three samples, featuring different hydraulic gradients, mean stresses, and stress ratios were selected from the experiments. It's noticed that in Eqs.(1)-(2), the seepage velocity of the specimen during suffusion is required. However, Liang et al. (Liang et al. 2017) did not provide the complete variation of seepage velocity, but only the final hydraulic gradient. Therefore, it is assumed that the flow velocity (v_f) remains constant and satisfies Darcy's law to obtain the required velocity for calculations based on the permeability coefficient provided in their study. Additionally, the model also requires the value of the maximum stress ratio M_p, which was also not provided in their experiments. Hence, it is assumed that its value is 1. It is important to note that these assumptions do not affect the correctness of the model; they only impact the calibration of parameter magnitudes. If an accurate value for M_p is available for the specimen, only the magnitude of the parameter needs to be adjusted accordingly.

Three groups of results with different hydraulic gradients, mean stresses, and stress ratios were selected and plotted in Fig. 7, where the dashed lines represent the predicted results from Eqs (1)- (2). The parameter values used in the calculations are shown in Table. 3. It can be observed that the proposed model successfully reproduces the main evolution of the experiments, indicating its effectiveness in capturing the suffusion process in gap-graded soils.

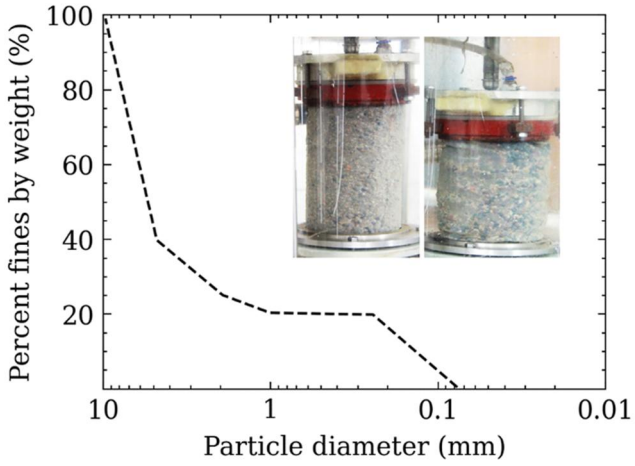

Fig. 6 PSD of soils and suffusion samples in the study of Liang et al.(Liang et al. 2017)

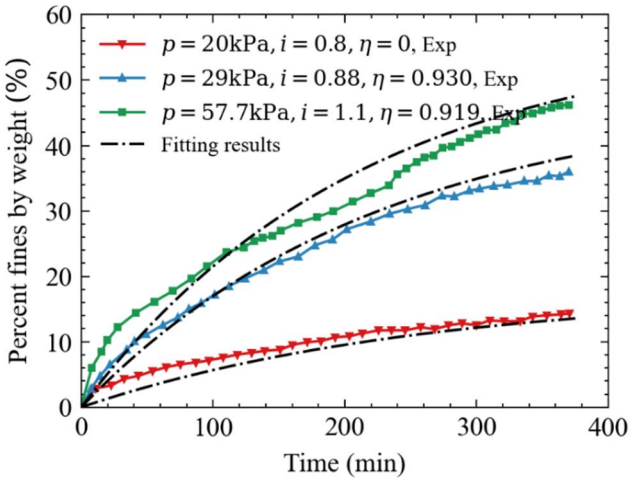

Fig. 7 Comparison of results from experiments and fitting

3 Hydromechanical framework for gap-graded soils

3.1 Four constituents model

The soil undergoing suffusion can be considered as a saturated soil. In previous studies, saturated soil has often been treated as a two-phase medium consisting of fluid and soil skeleton. However, erodible soils typically consist of coarse and fine particles. In this case, the fine particles can migrate within the pores with infiltrating water flow, while the coarse particles, serving as the soil skeleton, cannot be transported. Therefore, treating the soil as a two-phase medium fails to distinguish between the various modes of particle movement during erosion,

specifically for coarse and fine particles. Recently, Schaufler et al. (Schaufler et al. 2013) proposed a more detailed distinction within the solid phase of saturated soil, separating it into the soil skeleton composed of coarse particles, fluid-like fines, and solid-like fines. As shown in Fig. 8, in a representative elementary volume (REV) of saturated soil, the volume of solid (dV) consists of four constituents: pure fluid (n^{ff}), eroded fluidized fine particles (n^{fp}, fluid-like), non-eroded erodible fine particles (n^{se}, solid-like), and the coarse skeleton (n^{ss}). The volume fraction of each constituent is determined as follows:

$$n^i = \frac{\mathrm{d}V^i}{\mathrm{d}V} \tag{3}$$

where $i = \{ff, se, ss, fp\}$, V^i is the volume of each corresponding constituent. Then the mass balance equations for these four constituents can be derived, as shown in Eqs (4)-(7). The detailed derivation can be found in the studies by Schaufler et al. (Schaufler et al. 2013) and Yang et al. (Yang et al. 2019, 2020).

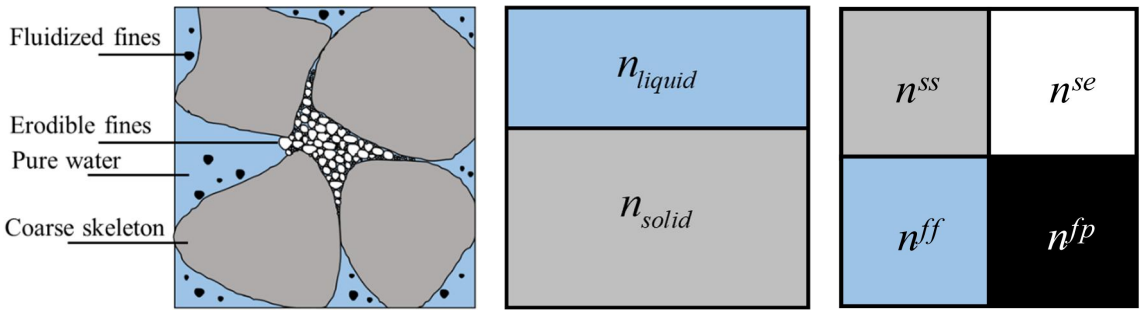

Fig. 8 Simplified modeling of saturated soils: (a) Mesoscale REV; (b) two-constituents continuum model; (c) four-constituents continuum model

$$-\frac{\partial \phi}{\partial t} + \mathrm{div}\left(\mathbf{v}_s\right) - \mathrm{div}\left(\phi \mathbf{v}_s\right) = \hat{n} \tag{4}$$

$$\frac{\partial(f_c)}{\partial t}-\frac{\partial(f_c\phi)}{\partial t}+\mathrm{div}(f_c\mathbf{v}_s)-\mathrm{div}(f_c\phi\mathbf{v}_s)=\hat{n} \tag{5}$$

$$\frac{\partial(c\phi)}{\partial t}+\mathrm{div}(c\mathbf{q}_\mathrm{w})+\mathrm{div}(c\phi\mathbf{v}_s)=-\hat{n} \tag{6}$$

$$\mathrm{div}(\mathbf{q}_\mathrm{w})+\mathrm{div}(\mathbf{v}_s)=0 \tag{7}$$

where "div" is the divergence operator. ϕ, c, and f_c are the porosity, concentration of the fluidized floating fines, and erodible fines content, respectively. $\hat{n}$ is the volume exchange rate, describing the transformation from erodible fines to the fluidized fines, which is introduced in the following section. $\mathbf{v}_s$ denotes the soil skeleton velocity. $\mathbf{q}_\mathrm{w}$ is the total discharge of the pore fluid. The porous flow is assumed to be governed by Darcy's law, therefore $\mathbf{q}_\mathrm{w}$ can be explicitly given by pore pressure p_w:

$$\mathbf{q}_\mathrm{w}=-\frac{k(f_c,\phi)}{\eta_k\bar{\rho}(c)}\mathrm{grad}(p_w) \tag{8}$$

where $k(f_c,\phi)$ denotes the intrinsic permeability of the medium, η_k is is the kinematic viscosity of the fluid, $\bar{\rho}(c)$ is the density of the mixture defined as:

$$\bar{\rho}=c\rho_s+(1-c)\rho_f \tag{9}$$

where ρ_s and ρ_f are the densities of solid and fluid, respectively. By specifying an appropriate erosion rate model $\hat{n}$, the system of partial differential equations can be solved.

3.2 Implementation of erosion law

The volume exchange rate $\hat{n}$ in Eqs (4)-(7), also known as the erosion law, represents the rate at which fine particles are eroded. It can be derived from the mass loss ratio m_e. Taking the derivative of Eqn.(1) yields:

$$\frac{\partial m_e}{\partial t}=\lambda v_f^a(p/p_{ref})^b m_\infty\exp(-\lambda v_f^a(p/p_{ref})^b t)=\lambda v_f^a(p/p_{ref})^b(m_\infty-m_e) \tag{10}$$

Then, based on the definition of the mass loss ratio, which is the ratio between the eroded fines mass Δm_f and the initial fines mass m_{f0}, m_e can be rewritten as follows:

$$m_e = \frac{\Delta m_f}{m_{f0}} = \frac{\Delta m_f}{m_0 f_{c0}} = \frac{\Delta m_f / \rho_s}{m_0 f_{c0} / \rho_s} = \frac{\Delta V_f}{V_0 f_{c0}} \tag{11}$$

where m_0 is the initial total mass of soil, f_{c0} is the initial fine content. ρ_s is the soil density. ΔV_f and V_0 denotes the cumulative volume of eroded fines and initial volume of soil, respectively. Similarly, differentiating Eqn. (9) yields:

$$\frac{\partial m_e}{\partial t} = \frac{1}{f_{c0}} \frac{\partial (\Delta V_f / V_0)}{\partial t} \tag{12}$$

Submitting $\hat{n} = \frac{\partial (\Delta V_f / V_0)}{\partial t}$ into Eqn.(10), the volume exchange rate can be expressed by:

$$\hat{n} = \lambda v_f^a (p / p_{ref})^b (m_\infty - m_e) f_{c0} \tag{13}$$

where m_∞ is the final mass loss ratio, given by Eqn.(2). $(m_\infty - m_e)$ denotes the residual fraction of the erodible fines.

Several researchers have proposed different erosion laws based on experimental results (Vardoulakis et al. 1996, Reddi et al. 2000, Steeb et al. 2007, Schaufler et al. 2013, Yin et al. 2020). However, these criteria often only consider erosion in relation to hydraulic gradient or seepage velocity. Nevertheless, both physical experiments (Chang and Zhang 2011, Chen and Zhang 2021) and numerical results (Liu et al. 2023) have demonstrated that the erosion law is also closely related to the stress state of the soil. In comparison to existing criteria, the newly proposed law (Eqn.(11) and Eqn. (2)) not only takes into account the seepage velocity but also incorporates the influence of mean stress p and stress ratio η (q / p). Consequently, it

provides a foundation for establishing a hydromechanical model that considers the suffusion process.

3.3 Critical state-based and fines-dependent mechanical model

In order to realise the hydromechanical modeling for suffusion, an appropriate mechanical constitutive model is of great importance. Yang et al.[19] pointed out that the influence of erosion on mechanical responses includes two aspects: first, the decrease of particles reduces the soil shear stiffness, leading to an increase in deformation of the granular assembly. Second, soil friction properties, for example, sliding resistance, can be changed due to erosion. Therefore, an exponential constitutive function proposed by Yin et al. [47,48], which integrates the effect of nonlinear elasticity, nonlinear stress dilatancy, critical state concept and interlocking effect is introduced in this study to characterize the mechanical properties of granular materials. A brief introduction to this model is presented in Appendix B, and more details can be found in (Jin et al. 2017, Yin et al. 2018, Wu 2019). The constitutive equations under axisymmetric triaxial conditions can be written as:

$$\delta p = K\left\{\delta\varepsilon_{\mathrm{v}} - A_{\mathrm{d}}\left(M_{\mathrm{pt}} - \frac{q}{p}\right)\delta\varepsilon_{\mathrm{d}}[1-\exp(-d\eta)]\right\} \tag{14}$$

$$\delta q = 3G\delta\varepsilon_{\mathrm{d}}\left(1-\frac{q}{pM_{\mathrm{p}}}\right)+\frac{q}{p}\delta p \tag{15}$$

where K and G denote the bulk moduli and shear moduli, respectively. $\delta\varepsilon_{\mathrm{v}}$ and $\delta\varepsilon_{\mathrm{d}}$ are volumetric and shear strain. M_{pt} is the slope of the phase transformation line. A_{d} and d are the stress-dilatancy parameters.

It's also worth noting that when fine particles within the soil are eroded, the porosity as

well as fine content vary correspondingly. Studies have illustrated that the mechanical response of gap-graded soils is highly dependent on fine content (Yin et al. 2014, 2016). In order to correctly reflect the mechanical variation induced by erosion, the above model can further be enhanced. Yin et al.(Yin et al. 2014) studied the behavior of sand-silt mixtures with varying fines content, and pointed out that fines content induces the motion of critical state line (CSL) in $e-\log p$ (Chang and Yin 2011, Xiong et al. 2020) of the soil mixtures. They concluded the critical model as:

$$e_{\mathrm{c}} = e_{\mathrm{cr0}} - \varsigma\left(\frac{p}{p_{\mathrm{at}}}\right)^{\xi} \tag{16}$$

$$\begin{aligned} e_{cr0} = &\left[e_{hc,cr0}\left(1-f_c\right)+m_1 f_c\right]\frac{1-\tanh\left[\zeta\left(f_c-f_{\mathrm{th}}\right)\right]}{2} \\ &+e_{hf,cr0}\left(f_c+\frac{1-f_c}{\left(R_d\right)^{m_2}}\right)\frac{1+\tanh\left[\zeta\left(f_c-f_{\mathrm{th}}\right)\right]}{2} \end{aligned} \tag{17}$$

where e_{c} is the critical state void ratio. p_{at} is atmospheric pressure. e_{cr0} is the reference critical void ratio at extremely low confining pressure. f_{th} is the threshold fines content from the coarse grains skeleton to the fine grains skeleton. ς and ξ are the material parameters determining the non-linearity of the CSL. $e_{hc,cr0}$ and $e_{hf,cr0}$ are the reference critical void ratios for the pure sand ($f_c=0$) and the pure silt ($f_c=100$), respectively. R_d is the ratio of the mean size of coarse particle and the mean size of fine particle. ζ controls the transition zone between the sandy silt and the silty sand. m_1 and m_2 are material constants.

Through the aforementioned model, it can be observed that, on one hand, the variations in soil stiffness and strength are related to the changes in void ratio induced by particle loss (see Appendix B). On the other hand, the soil critical state line can also shift with the fine

content during erosion (see Eqs. (16)-(17)).

3.4 Numerical scheme of hydromechanical modeling

It's noticed that the framework in this study realizes the two-way full coupling between erosion and mechanical response. On the one hand, the stress state of the soil is considered through the proposed erosion law, which controls the erosion evolution. On the other hand, the effect of erosion on mechanical behaviour is considered through two aspects. Firstly, the erosion-induced f_c variation is directly linked to the position of CSL in the constitutive model. Secondly, erosion-induced void ratio increase also changes the soil's peak strength and stiffness. Using the above framework, the hydromechanical modeling can be implemented for internal erosion tests. Unlike the traditional triaxial experiments, the soil specimen during the erosion test is normally subjected to constant boundary stresses. Therefore, the strain change is actually induced by the variation of peak strength ratio and stiffness, as:

$$\delta\varepsilon_{\mathrm{d}} = -\left(\frac{M_{\mathrm{p}}}{G_{\eta}}\ln\left[\frac{M_{\mathrm{p}}-\eta}{M_{\mathrm{p}}}\right]\right)^{(i)} + \left(\frac{M_{\mathrm{p}}}{G_{\eta}}\ln\left[\frac{M_{\mathrm{p}}-\eta}{M_{\mathrm{p}}}\right]\right)^{(i-1)} \tag{18}$$

$$\delta\varepsilon_{\mathrm{v}} = -\frac{p}{K^2}\delta K + A_{\mathrm{d}}\left(M_{\mathrm{pt}} - \frac{q}{p}\right)\delta\varepsilon_{\mathrm{d}}[1-\exp(-d\eta)] \tag{19}$$

where the superscript (i) represents the current loading step and $(i-1)$ is the previous loading step. The incremental void ratio also includes two parts, e.g., the void ratio induced by the body deformation and fine particle volume loss caused by erosion, given:

$$(\delta e)_{\mathrm{total}} = (\delta e)_{\mathrm{erosion}} + \delta\varepsilon_{v}(1+e) \tag{20}$$

Through the given boundary conditions and erosion law $\hat{n}$, the aforementioned partial differential equations are explicitly solved in time and by the FDM (i.e., finite difference

method) in space. At the timestep i, the value of skeleton displacement $\mathbf{u}_s^{i-1}$ (note that soil solid velocity v_s^{i-1} can be explicitly derived through $\mathbf{u}_s^{i-1}$), the pore pressure p_w^{i-1}, the porosity ϕ^{i-1}, the fines content f_c^{i-1}, and the concentration of fluidized particles c^{i-1} of timestep $(i-1)$ are used to calculate p_w^i, ϕ^i, f_c^i and c^i through Eqs.(4)-(8). Afterwards, p_w^i, ϕ^i, f_c^i and c^i are incorporated into Eqs.(18)-(19) to update the soil strain increment ($\delta\varepsilon_{\mathrm{d}}^i$ and $\delta\varepsilon_v^i$) and $\mathbf{u}_s^i$. Then, the obtained $\mathbf{u}_s^i, p_w^i$, ϕ^i, f_c^i and c^i, as an initial condition, can be used for the next loop until the end of the modeling.

4 Validation and discussion

The framework presented in Section 3 is highly suitable for conducting triaxial suffusion tests, which involve subjecting soil to constant stress while observing erosion processes. It is noticed that Chang et al. (Chang and Zhang 2011, 2013a) conducted suffusion tests using an adapted stress-controlled erosion apparatus. The evolution of suffusion under complex stress states, as well as the soil stress-strain response subjected to suffusion are presented in their study, which can be used to validate the numerical model in this study.

4.1 Description of laboratory suffusion tests

Chang et al. (Chang and Zhang 2011, 2013a) carried out the suffusion tests on gap-graded HK-CDG granular soil, with the GSD shown in Fig. 1. The samples, measuring 100mm in height and 100mm in diameter, were initially subjected to isotropic compression to achieve a predetermined confining pressure. Subsequently, the vertical stress was increased to induce an anisotropic stress state. Upon completion of the loading phase, a seepage flow, parallel to the principal stress of the sample, was introduced through a water supply system connected to the

365 triaxial apparatus. The applied water pressure followed a non-uniformly varying pattern. As is
366 illustrated in Fig. 9, each stage of the hydraulic gradient within the sample lasts 10 mins, and
367 the increase magnitude is 0.15 m/m for $i \le 1.0$ m/m, 0.25 m/m for $1.0 \text{ m/m} < i < 2.0$ m/m,
368 and 0.50 m/m for $i > 2.0$ m/m. For each gradient level, the hydraulic pressure was increased
369 within the first 2 minutes and then kept constant for the following 8 minutes to ensure there
370 was no more soil loss. Throughout the suffusion process, the external stress remained constant,
371 while the weight of the eroded mass and the outflow rate were continuously monitored. Fig. 10
372 presents the deformation of the sample before and after suffusion. Detailed soil properties such
373 as density, initial void ratio, and hydraulic conductivity can be found in the works of Chang
374 and Zhang (Chang and Zhang 2011, 2013a).

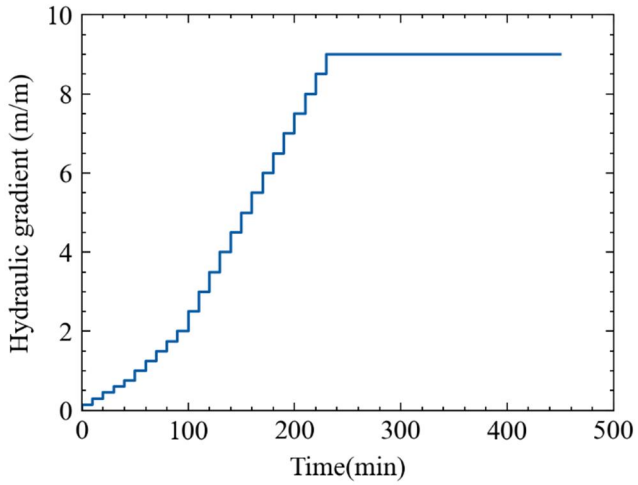

375
376 Fig. 9 Hydraulic gradient applied during suffusion tests

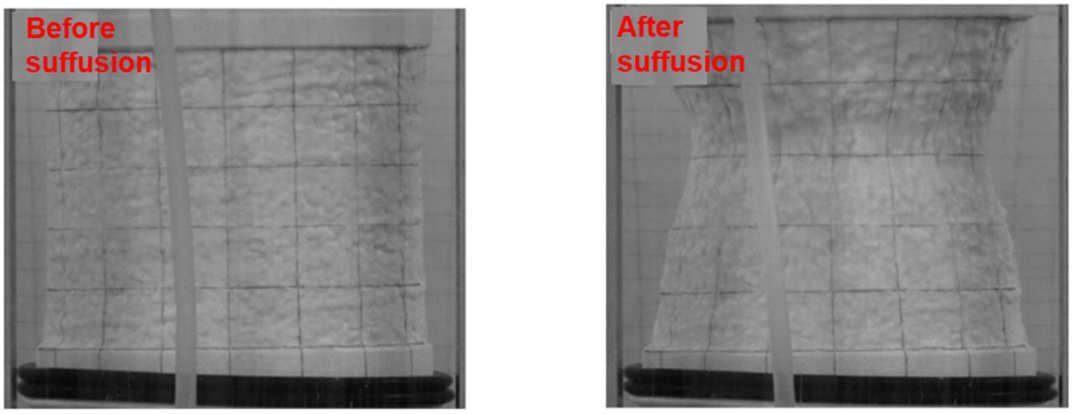

377 Fig. 10 Deformation of specimen before and after suffusion (Chang and Zhang (Chang and Zhang 2013a))

378 Prior to conducting hydromechanical calculations, it is essential to calibrate the
379 parameters involved in the model, which include soil physical parameters, mechanical
380 parameters (K_0, G_0, n, d, A_d , ϕ_c in Eqs.(B1)-(B5)), CSL-related parameters (ς, ξ ,
381 $e_{hc,cr0}, m_1, \zeta, f_{th}, e_{hf,cr0}, m_2, R_d$ in Eqs.(16)-(17)), and erosion-related parameters
382 ($\lambda, a, b, c, k_1, k_2, k_3, v_{fc}$ in Eqs.(1)-(2)). The soil physical parameters can be directly obtained
383 from the values provided in the experiments. The mechanical parameters can be determined by
384 fitting the stress-strain relationships reported in the triaxial tests conducted by Chang and
385 Zhang (Chang and Zhang 2013a) (the fitting results can be found in (Yang et al. 2020)).
386 However, the determination of CSL-related parameters is more complex due to limited
387 experimental data. Fortunately, Yin et al.(Yin et al. 2014) have conducted a series of
388 experiments on soil critical state for coarse-fine mixtures, which are similar to gap-graded soils,
389 aligning well with the objectives of this study. Therefore, the CSL-related parameters are fitted
390 using the results obtained by Yin et al. (Yin et al. 2014). For example, Fig. 11 illustrates the
391 fitting results compared to the experiments using Eqn. (17). Furthermore, some scholars (Jin et
392 al. 2018) have also developed optimization methods for the determination of the mechanical
393 parameters, and more information can be found in their related studies. For the erosion-related

parameters, they can be determined by fitting the mass loss results reported in the experiments (Chang and Zhang 2013a). All the parameters used in the model are summarized in Table.4.

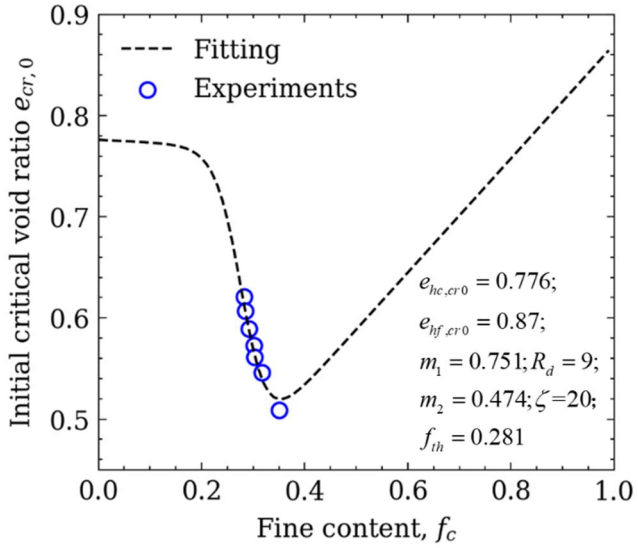

Fig. 11 Determination of CSL related parameters

4.2 Comparison between simulations and experiments

According to the previous calculation scheme and determined parameters, the simulation results are obtained and compared with the results from experimental samples GS-C-1, GS-C-5, GS-C-6 (Chang 2012), as shown in Fig. 12. The erosion tests for these samples were conducted with a confining stress of 50 kPa and deviatoric stresses of 0, 100, and 150 kPa, corresponding to stress ratios of $\eta = 0$, 1.2 and 1.5, respectively. Fig. 12(a) presents the cumulative eroded soil weights for these tests. It is clear that the eroded mass rises with the stress ratio, highlighting the substantial impact of stress state on erosion. This trend can be attributed to the loss of fine particles, which triggers a reconfiguration of the soil microstructure. As a result, the soil transitions from an anisotropic state to an isotropic state (Zhou et al. 2022, Liu et al. 2023). Therefore, a more pronounced initial stress anisotropy leads

410 to a more intense particle adjustment, resulting in a greater amount of mass loss. The findings
411 indicate that the proposed model effectively replicates the overall erosion evolution process,
412 with the final eroded mass at the stable stage increasing in line with the stress ratio. Furthermore,
413 it should be noted that for sample GS-C-1 under isotropic stress, the mass loss exhibits a sharp
414 increase between Time=100-180 min, and the simulation results successfully capture this
415 significant rise during the same time period. However, there are also noticeable discrepancies
416 between the model and the experimental results for samples GS-C-5 and GS-C-6 under
417 anisotropic stress states. The model fails to accurately capture the turning point (i.e., critical
418 gradient) that corresponds to the abrupt change in eroded mass. Specifically, the mass loss of
419 sample GS-C-5 begins to increase rapidly around Time=200 min, whereas the model predicts
420 this increase at around Time=120 min. There are several possible reasons for these
421 discrepancies. Firstly, the erosion law adopted in the model is derived from CFD-DEM
422 simulations. However, it has been suggested by Cheng et al. (Cheng et al. 2021) that such
423 unresolved CFD-DEM simulations may not provide accurate results for determining the critical
424 gradient. Secondly, the numerical model utilizes the finite difference method, treating the soil
425 as a representative elementary volume, and does not consider the spatial inhomogeneity of the
426 soil. In contrast, soil samples in the experiments inherently possess variations in void ratio and
427 fine content, leading to deviations from the model predictions.
428
429
430
431
432
433

434

Table. 4 Parameters used in the hydramechanical model

Physical properties of HK-CDG soil	Density of fluid	ρ_f	1.00g/cm^3
	Density of soil	ρ_s	2.65g/cm^3
	Kinematic viscosity of fluid	η_k	$5.0\times10^{-6} m^2/s$
	Initial fines content	f_{c0}	0.35
	Initial permeability	k_0	$7.5\times10^{-5} m/s$
	Initial void ratio	e_0	0.53
Mechanical constants of HK-CDG mixture	Elastic parameters	K_0	50MPa
		G_0	16.7MPa
		n	0.95
		n_p	4
		n_d	10
	Dilatancy parameters	d	18
		A_d	0.35
	CSL-related parameters	$e_{hc,cr0}$	0.776
		$e_{fc,cr0}$	0.87
		ξ	0.45
		λ	0.03
		m_1	0.751
		m_2	0.474
		ϕ_c	40.5
Erosion model parameters	Erosion rate controlling parameters	λ	1
		a	0.87
		b	-1.5
	Final mass loss controlling parameters	m_0	3.84
		c	8
		k_1	-0.05
		k_2	0.7
		k_3	-0.4
		v_{fc}	4.2 cm/s

435

436

Fig. 12(b) illustrates the evolution of hydraulic conductivity. It is observed that after erosion occurs, the permeability of the soil increases as the particles decrease. Experimental findings indicate that after reaching its peak, the permeability decreases during the later stages of seepage erosion. When compared with numerical models, the proposed model in this study accurately predicts the growth process of permeability and the peak values achieved by the specimens under different stress conditions. However, unlike the experiments, the model-calculated permeability maintains a nearly constant value after reaching the peak, without exhibiting a decrease. This discrepancy can be attributed to the occurrence of local clogging within the specimens. In actual seepage processes, fine particles can be lost through the pores of the soil skeleton, but they can also undergo self-filtration, leading to the aggregation of fine particles within the pores and reducing local permeability. Unfortunately, the numerical model does not consider the heterogeneity of the specimens and thus is unable to account for local clogging phenomena or accurately reflect the decrease in permeability observed during the later stages of erosion.

Fig. 12 (c)-(d) depicts the axial and radial strain induced by erosion. It is observed that soil deformation becomes more pronounced with increasing stress ratio. In general, the proposed model effectively captures both the rapid deformation phase and the subsequent stable stage of soil. However, it should be noted that there are still discrepancies observed for certain samples, such as sample GS-C-5. There are two main reasons for this discrepancy. Firstly, the parameters related to mechanical behavior in the model were fitted from a similar study, rather than directly from HK-CDG data, due to the lack of available data. This difference

in parameter selection could affect the model's ability to accurately estimate the strains. Secondly, in the erosion tests, the stress state was maintained constant throughout, implying that the strains are solely influenced by the eroded particles. As mentioned earlier, there are differences in the cumulative mass loss results between the model and experiments. Consequently, the strains predicted by the model also exhibit slight variations compared to the experimental data.

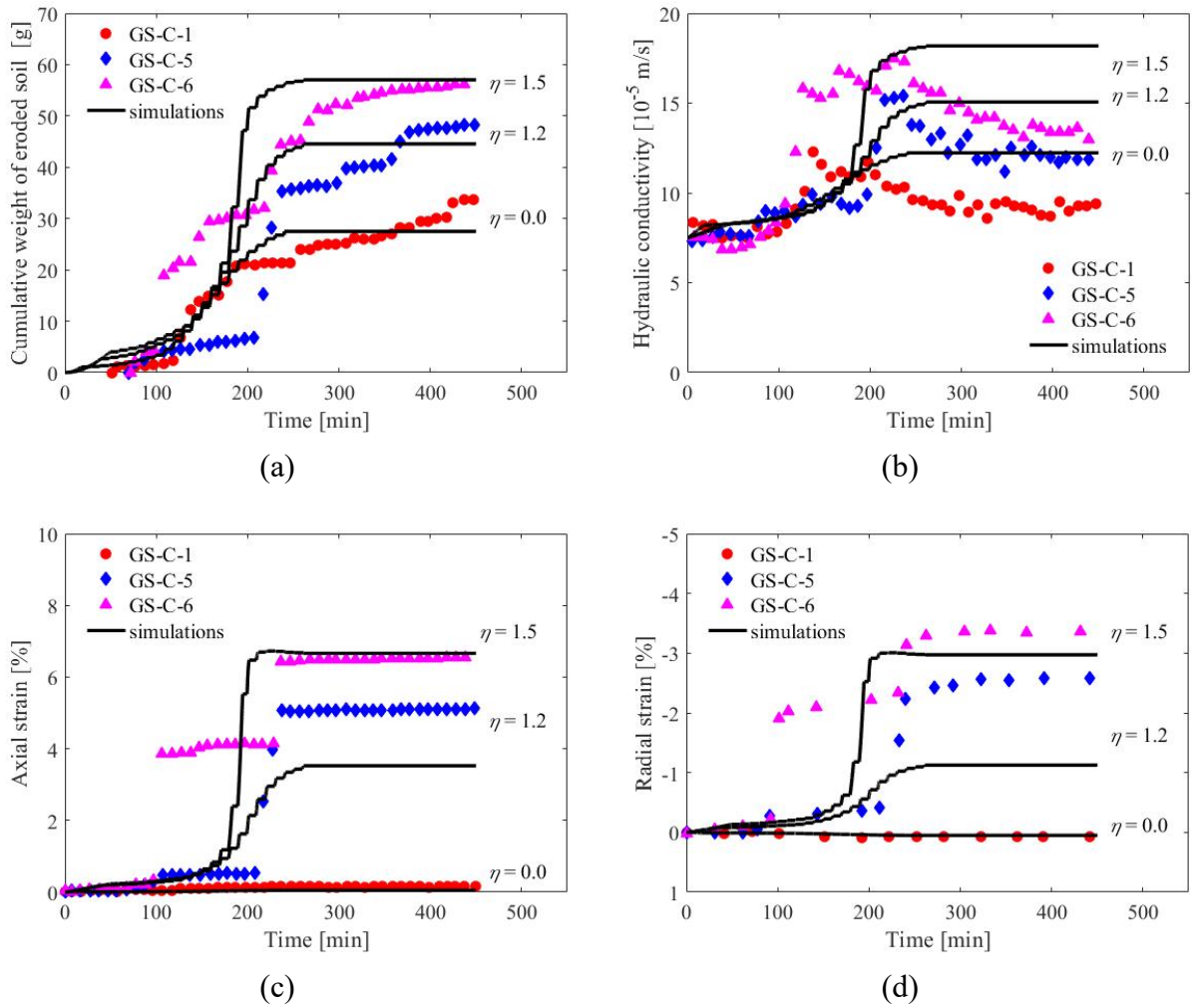

Fig. 12 Comparison between experiments and numerical simulations: (a) cumulative mass; (b) evolution of hydraulic conductivity; (c) axial strain; (d) radial strain

It is worth mentioning that Yang et al.(Yang et al. 2020) have made an attempt to

incorporate the influence of shear stress into the erosion law proposed by Uzuoka et al.(Uzuoka et al. 2012). Therefore, Fig. 13 compares the erosion law proposed in this study with the one proposed by Yang et al and Uzuoka et al. The results show that under zero stress ratio, both models yield similar calculations. However, Uzuoka et al.'s model can not estimate the results for anisotropic stress conditions, and the accuracy of Yang et al.'s model diminishes under high stress ratios. It becomes challenging for their model to adequately capture the differences in cumulative mass loss and variations in permeability coefficient between the two groups of models, i.e., $\eta = 1.2$ and $\eta = 1.5$. Furthermore, it can be observed that all these models suffer from the same limitation of not considering particle clogging effects and non-uniformity. Consequently, there are discrepancies between the model predictions and experimental data regarding changes in the hydraulic permeability coefficient during the later stages of erosion. This highlights the need for improvement in future models to better account for these factors.

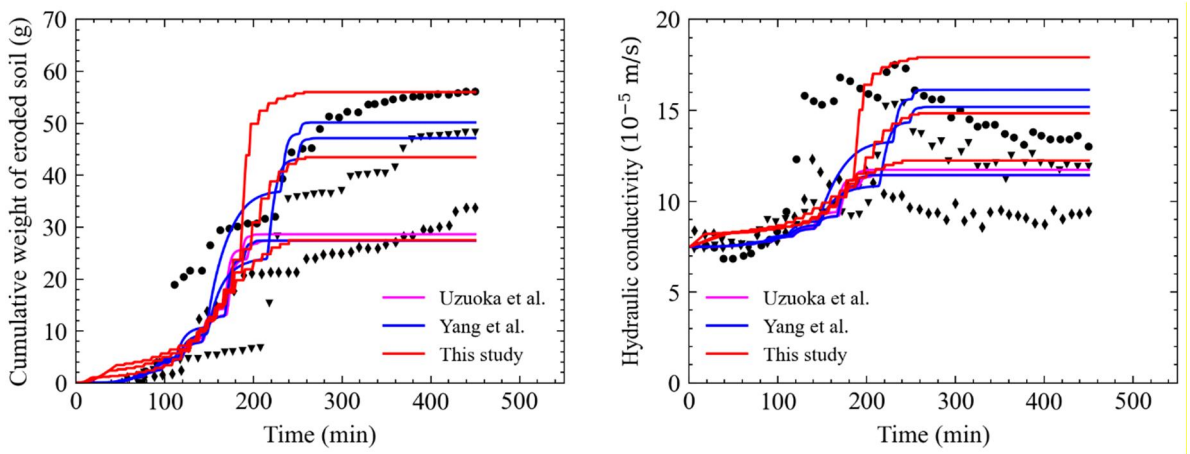

(a) Eroded soil mass (b) Hydraulic conductivity

Fig. 13 Comparison of different erosion laws

4.3 Influence of soil initial state on suffusion response

The analysis conducted above provides compelling evidence for the efficacy of the erosion model based on CFD-DEM, in conjunction with the hydromechanical framework presented in

484 this study, to accurately capture the fundamental features of soil subjected to suffusion.
485 Consequently, a series of additional erosion simulations is carried out to explore the impact of
486 various influencing factors.

487 Fig. 14 (a) depicts the mass loss of soils with different void ratios e_0, revealing that denser
488 samples exhibit lower mass loss under the same stress conditions. In the proposed model, the
489 direct incorporation of void ratio into the erosion law is not employed. Instead, void ratio is
490 considered in the calculation of CSL, mechanical stiffness, and hydraulic velocity. A higher
491 void ratio results in increased hydraulic conductivity and, consequently, a larger seepage
492 velocity under the same input gradient. Additionally, the influence of soil friction angle is
493 investigated and presented in Fig. 14(b). It is observed that a higher friction angle leads to
494 increased resistance to erosion. Furthermore, the mass loss gradually decreases with larger
495 friction angles, whereas at smaller friction angles, the soil sample undergoes more deformation
496 at the same stress level, resulting in a sudden surge in mass loss, for instance, at $\phi_c = 33^\circ$ and
497 T = 200min. Fig. 14(c) illustrates the impact of initial fines content f_{c0} on erosion, revealing
498 that it not only affects the final mass loss but also the temporal progression of erosion. The
499 cumulative mass loss increases with higher fines content. Moreover, as fine content increases,
500 the soil transitions from an underfilled to an overfilled state, causing fine particles to participate
501 in more stress transfer and consequently exhibit greater erosion resistance. As a result, samples
502 with higher fines content initiate suffusion at a relatively later stage compared to those with
503 lower fines content, demonstrating that greater hydraulic gradients are required to induce
504 particle migration in overfilled soils. Fig. 14(d) investigates the influence of size ratio R_d,

505 defined as the ratio of coarse to fine particle sizes, on the erosion process. This exploration is
506 motivated by the significant impact of the coarse-to-fine particle ratio on soil properties in gap-
507 graded mixtures. The results obtained demonstrate that the current hydromechanical coupling
508 model effectively captures the mass loss variations corresponding to different size ratios.
509 Specifically, as the size ratio increases, the mass loss also exhibits an increasing trend. Xie et
510 al. (Xie et al. 2023) also noted that the larger the size ratio, the less contribution is made by the
511 fine particles in bearing forces. Consequently, the resistance to erosion decreases, leading to
512 higher mass loss.

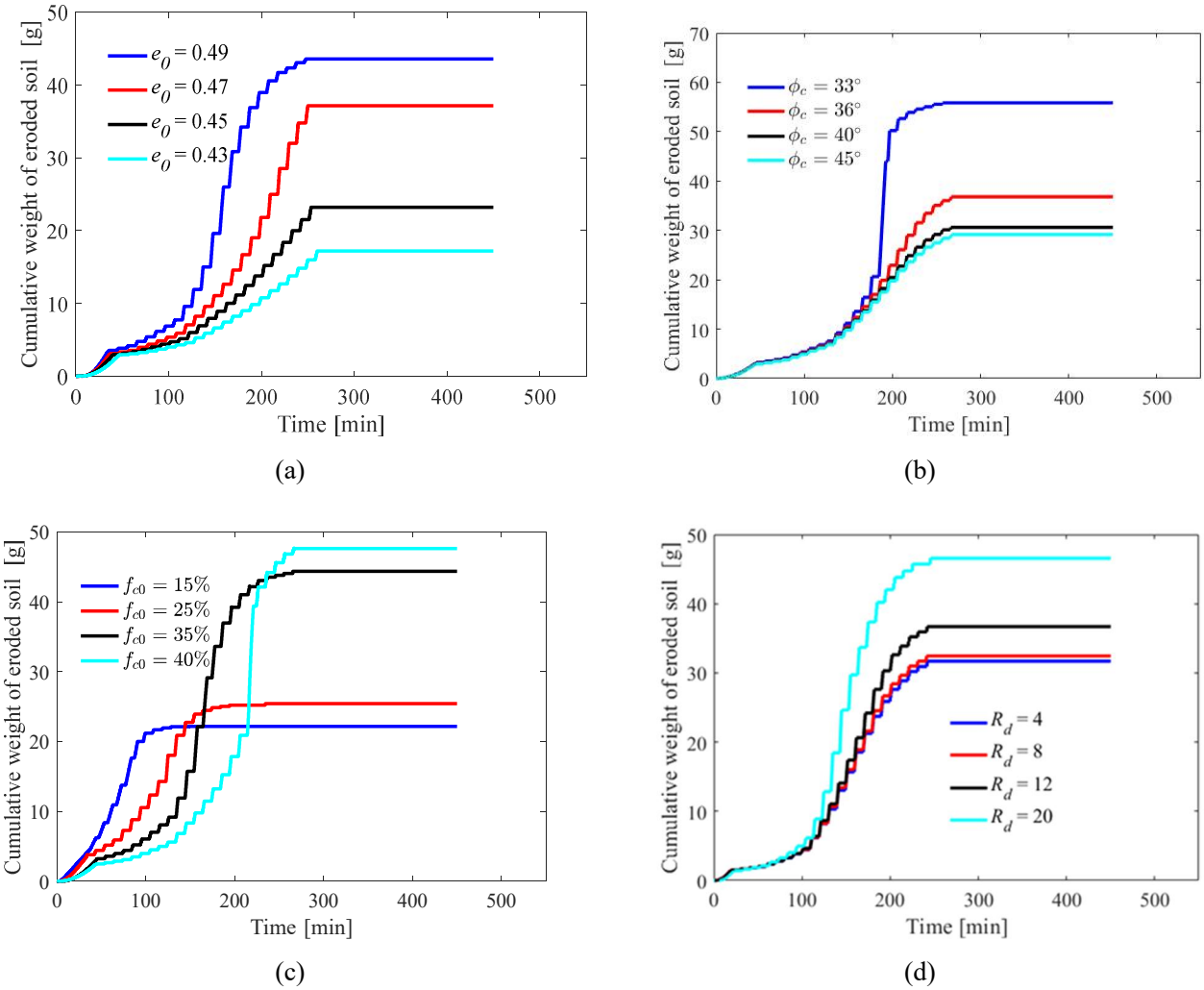

513 Fig. 14 Cumulative mass loss for samples with different (a) void ratio; (b) friction angle; (c) size ratio

4.4 Soil mechanical response subjected to suffusion

Previous studies (Ke and Takahashi 2014b, Qian et al. 2021) have reported variations in soil strength subsequent to erosion. In this section, drained triaxial tests are simulated on pre- and post-suffusion samples to investigate the effect of soil strength by erosion using existing models. Samples with different initial void ratios and fine contents were selected and subjected to shear tests.

Fig. 15(a) presents the relationship between deviatoric stress and axial strain prior to erosion, indicating a transition from a hardening to a softening stress-strain behavior with decreasing initial void ratio. This shift corresponds to a transformation from dilative behavior to contractive behavior, as demonstrated in Fig. 15(b). Upon erosion, a significant decrease in the peak strength of the soil specimens is observed. Specifically, the stress-strain curves of initially dense specimens ($e_0 = 0.43, 0.45,$ and 0.47) shift from a softening-type behavior prior to erosion to a hardening-type behavior, accompanied by a notable reduction in peak strength. For instance, the specimen with an initial void ratio of 0.43 displays a peak strength of approximately 330 kPa before erosion, which decreases to around 230 kPa after erosion. Meanwhile, no shear dilative behavior is observed in the change of void ratios for these samples subsequent to erosion. However, it is important to note that the initially loose specimen ($e_0 = 0.49$) exhibits a slight increase in strength after erosion, along with a minor shear dilative response in the change of void ratios. These observations can be attributed to two key factors influencing the mechanical behavior of the soil post-erosion. Firstly, the loss of mass during erosion leads to an enlargement of the void ratios, consequently resulting in a reduction in soil

strength. Conversely, for gap-graded soils, when the fine content f_c falls below a certain threshold value (typically f_c = 35%), a decrease in f_c actually leads to an increase in soil strength (Shire et al. 2014, Yin et al. 2014, Taha et al. 2019). As a result, initially dense specimens are more susceptible to the increase in void ratios after erosion, which significantly reduces their strength. In contrast, initially loose specimens are less affected by changes in void ratios, and the decrease in f_c enhances force transmission through the coarse skeleton, thereby leading to an increase in soil strength. In order to validate the above findings, the influence of the initial fine content f_{c0} on the mechanical response is analyzed using the framework. As is illustrated in Fig. 16, the soil strength decreases with an increase in f_{c0} when f_{c0}<35% prior to erosion, whereas it increases with an increase in f_{c0} when f_{c0}>35%. Such non-linear variation corresponds well with previous studies (Shire et al. 2014, Yin et al. 2014, Taha et al. 2019). Moreover, the samples with a fine content of 15%, 25% and 40% show the shear dilatancy in void ratio, while the sample with a fine content of 35% shows the shear contraction. Following erosion, the initially dense sample (f_{c0} = 15%, 25%, and 40%) also displays a reduction in strength, whereas the initially loose sample (f_{c0} = 35%) exhibits a slight increase in strength.

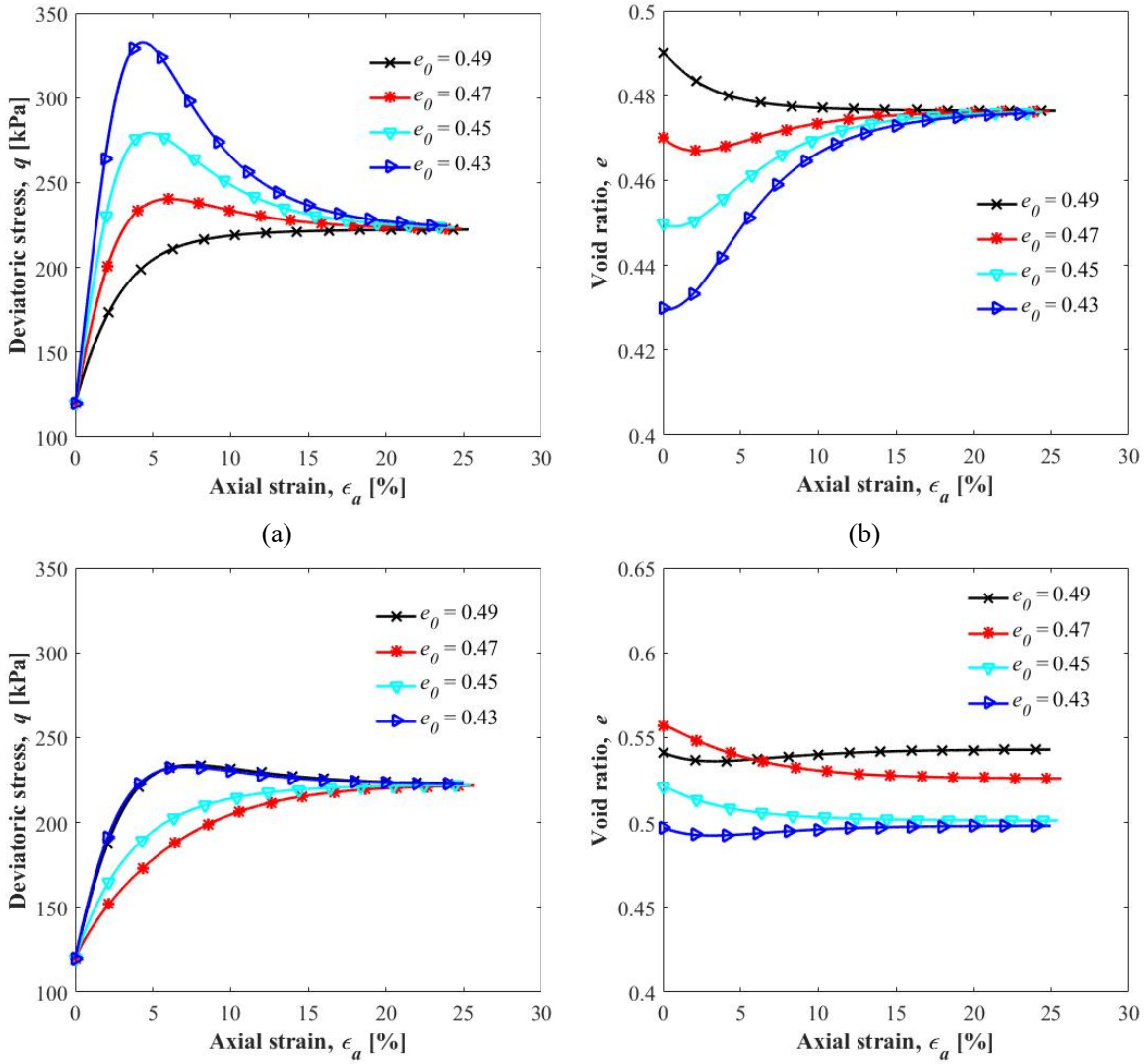

Fig. 15 Results of drained triaxial tests for the sample with different void ratios before and after erosion: (a,c) deviatoric stress versus axial strain; (b,d) void ratio versus axial strain.

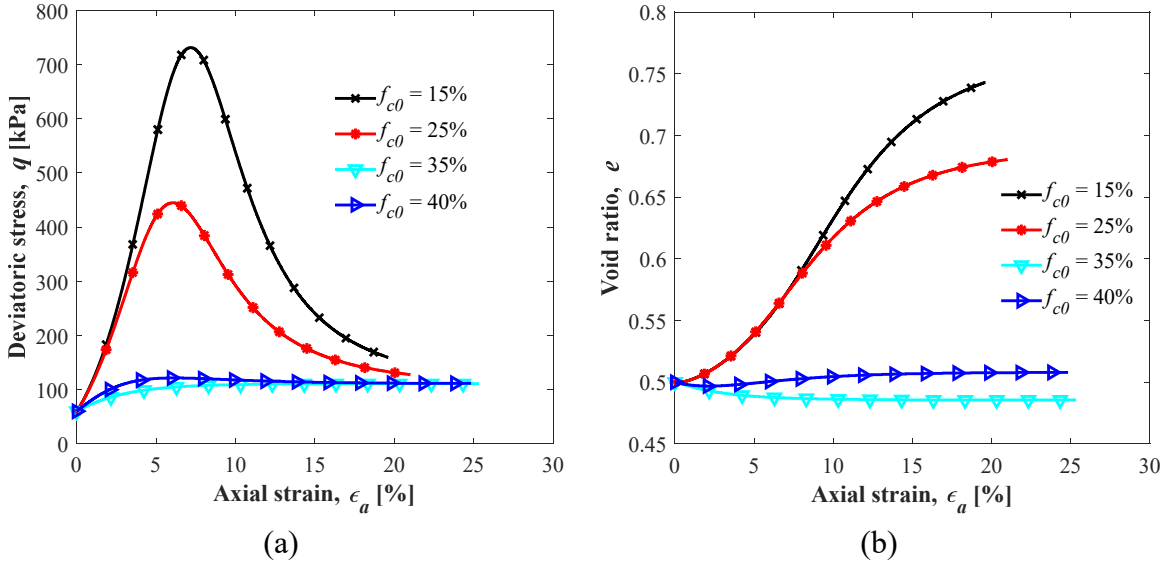

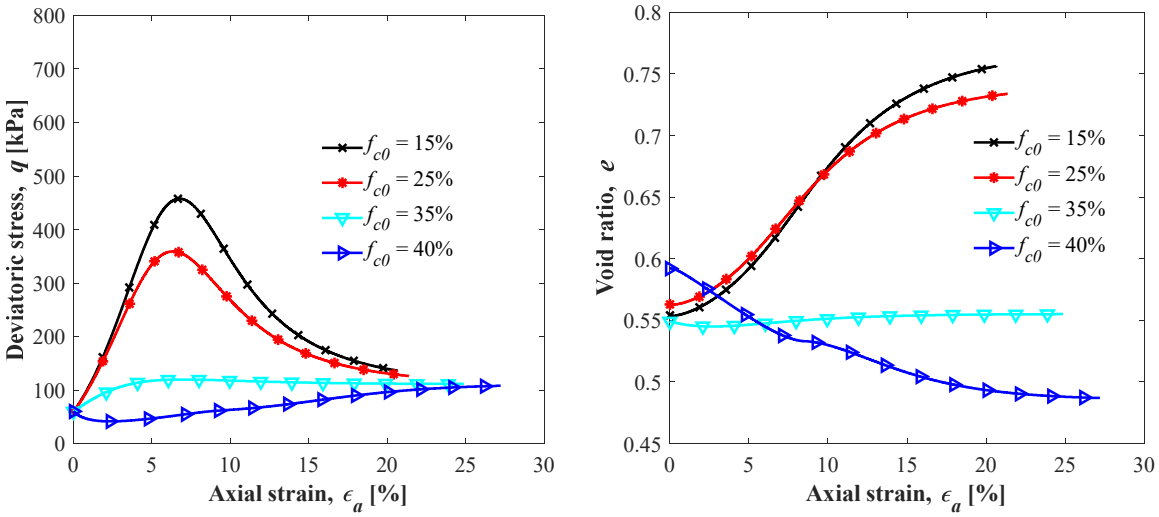

(c) (d)

Fig. 16 Results of drained triaxial tests for sample with different fine contents before and after erosion: (a,c) deviatoric stress versus axial strain; (b,d) void ratio versus axial strain.

5 Conclusion

In this study, a novel erosion law has been proposed based on simulation results obtained from coupled CFD-DEM models. The erosion law takes into account both hydraulic conditions and soil stress states. Subsequently, it was integrated into a four-constituent continuum model, coupled with a critical state-based fines-dependent constitutive model, enabling the realization of hydromechanical modeling of gap-graded soils with suffusion. To validate the proposed erosion with the framework, a series of erosion tests was simulated and compared with experimental data. Furthermore, the model was utilized to investigate the influence of significant factors on erosion evolution and the subsequent variation in soil strength after erosion. The key findings and conclusions are summarized as follows:

(1) According to the CFD-DEM simulations, an exponential model is found appropriate to represent evolution of mass loss induced by erosion for samples under different seepage velocities, mean stress and shear stress ratios. By a set of appropriate parameters, the

568 experimental observation can be well captured using the proposed erosion model.

569 (2) The established hydromechanical model achieves a two-way coupling between erosion
570 and soil mechanical behavior. It incorporates the influence of stress on erosion through the
571 erosion rate, while also accounting for the impact of erosion on stress through the fine content-
572 related critical state theory. As a result, this framework effectively captures the essential
573 characteristics of suffusion specimens subjected to various stress states and hydraulic
574 conditions.

575 (3) The current framework effectively showcases the influence of multiple factors on
576 suffusion phenomena, underscoring its wide applicability in the field of suffusion analysis.
577 Moreover, it successfully captures the variations in soil mechanical response resulting from
578 suffusion. Drained triaxial tests reveal that erosion has a detrimental impact on the initial dense
579 soil sample, leading to a reduction in soil strength. Conversely, for the initial loose sample,
580 erosion exhibits a subtle enhancement in peak strength.

581 (4) The findings of this study demonstrate the successful utilization of the CFD-DEM
582 simulations-based erosion law in hydromechanical modeling. Remarkably, the developed
583 model is incorporated within the continuum medium framework, indicating the feasibility of
584 solving governing equations through various numerical methods, such as finite difference or
585 element methods.

586 Although the overall results demonstrate a reasonably satisfactory agreement, it is
587 important to acknowledge that the absence of considering sample inhomogeneity may
588 introduce certain discrepancies. This highlights the need for future studies to explore and

address this aspect to further enhance the model's accuracy and applicability.

Data Availability Statement

All data that support the findings of this study are available from the corresponding author upon reasonable request.

Declaration of interests

The authors declare that they have no known competing financial interests or personal relationships that could have appeared to influence the work reported in this paper.

Acknowledgments

The financial supports provided by the GRF project (Grant No. 15209119, 15226322, 15229223) from the Research Grants Council (RGC) of Hong Kong, the National Natural Science Foundation of China (Project No. 52178345), and Fundamental Research Funds for the Central Universities （2023-2-ZD-08) are gratefully acknowledged.

Appendix A. Methodology of coupled CFD-DEM

Governing equations

The CFD-DEM calculations are realized by the following governing equations, where Eqs. A1-A2 describe the particle motion according to Newton's motion laws, and Eqs. A3-A4

describe the fluid velocity and pressure according to the averaged Navier–Stokes equation:

$$m_i \frac{\mathrm{d}\mathbf{v}_i}{\mathrm{d}t} = \sum_{j=1}^{N} \mathbf{f}_i^j + \mathbf{f}_i^{f\to p} \tag{A1}$$

$$I_i \frac{\mathrm{d}\boldsymbol{\omega}_i}{\mathrm{d}t} = \sum_{j=1}^{N} \mathbf{M}_i^j + \mathbf{M}_i^{f\to p} \tag{A2}$$

$$\frac{\partial \rho_f \alpha_f}{\partial t} + \nabla \cdot \left(\rho_f \alpha_f \mathbf{u}_f \right) = 0 \tag{A3}$$

$$\frac{\partial \left(\alpha_f \rho_f \mathbf{u}_f \right)}{\partial t} + \nabla \cdot \left(\alpha_f \rho_f \mathbf{u}_f \mathbf{u}_f \right) = -\alpha_f \nabla p + \nabla \cdot \left(\alpha_f \tau_f \right) + \mathbf{f}^{p\to f} \tag{A4}$$

where m_i is the mass of particle i , and I_i denotes the moment of inertia. $\mathbf{v}_i$ is translational velocity, and $\boldsymbol{\omega}_i$ is the angular velocity. $\mathbf{f}_i^j$ and $\mathbf{M}_i^j$ represent the contact force and torque between particle i and j. N is the total contact number. $\mathbf{f}_i^{f\to p}$ is the interaction force exerted on particle by the flow. $\mathbf{M}_i^{f\to p}$ is torque from the fluid velocity gradient. α_f is the fluid volume fraction for each fluid cell. p is the averaged pressure, and $\mathbf{u}_f$ is the averaged velocity of the fluid. ρ_f and τ_f are fluid density and shear stress tensor of the fluid, respectively. $\mathbf{f}^{p\to f}$ is the interaction force exerted on flow by the particles, which is given by $\mathbf{f}^{p\to f} = -\dfrac{\sum_{p=1}^{N} \mathbf{f}^{f\to p}}{V_c}$, and V_c is the cell volume.

Appendix B. Critical state-based constitutive model

The constitutive model is developed based on an exponential frictional model by implementing the nonlinear elasticity, nonlinear stress dilatancy and critical state concept (Yin et al. 2018, Wu et al. 2019). The elasticity is given:

$$\delta\varepsilon_{ij}^{e}=\frac{\delta\sigma^{'}}{2Gij}-\frac{v\delta\sigma^{'}_{kk}\delta_{ij}}{2G(1+v)} \tag{B1}$$

$$G=G_0 p_{at}\frac{(2.97-e)^2}{(1+e)}\left(\frac{p^{'}}{p_{at}}\right)^{n} \tag{B2}$$

$$K=K_0 p_{at}\frac{(2.97-e)^2}{(1+e)}\left(\frac{p^{'}}{p_{at}}\right)^{n} \tag{B3}$$

622 The yield function is

$$f_s=p/q'-M_p\left(1-e^{-\frac{G_\eta}{M_p}\varepsilon_d}\right) \tag{B4}$$

623 The nonlinear stress dilatancy is

$$\frac{\delta\varepsilon_v^{p}}{\delta\varepsilon_d}=A_d\left(M_{pt}-\frac{q}{p^{'}}\right)\delta\varepsilon_d[1-\exp(-d\eta)] \tag{B5}$$

624 The critical state line and interlocking effect are

$$e_{\mathrm{c}}=e_{\mathrm{cr0}}-\varsigma\left(\frac{p}{p_{\mathrm{at}}}\right)^{\xi} \tag{B6}$$

$$\tan\phi_p=\left(e_c/e\right)^{n_p}\tan\phi_c;\quad \tan\phi_{pt}=\left(e/e_c\right)^{n_d}\tan\phi_c \tag{B7}$$

$$M_p=6\sin\phi_p/\left(3-\sin\phi_p\right);\quad M_{pt}=6\sin\phi_{pt}/3-\sin\phi_{pt} \tag{B8}$$

625 where $p^{'}$ is is the mean effective stress. G_0 is reference bulk moduli, and K_0 is
626 reference shear moduli. e denotes the current void ratio. p_{at} is the is the atmospheric
627 pressure. n represents a nonlinear elastic constant. M_p is peak stress ratio. k_p represents
628 plastic modulus. A_{d} and d is a constant controlling the magnitude of the stress-dilatancy.
629 e_{c} is the critical state void ratio. e_{cr0} is the reference critical void ratio at extremely low
630 confining pressure. ς and ξ are the material parameters determining the non-linearity of
631 the CSL. ϕ_{p} and ϕ_{pt} are peak friction angle and phase transition angle. ϕ_c is friction angle.

632 n_p and n_d are model interlocking parameters.

633

Reference

Ai, J., Chen, J.-F., Rotter, J.M., and Ooi, J.Y. 2011. Assessment of rolling resistance models in discrete element simulations. Powder Technology, **206**(3): 269–282.

Azadbakht, S., Nouri, A., and Chan, D. 2020. An analytical model for estimation of internal erosion rate. Geomechanics and geoengineering: an international journal, **15**(1): 42–53.

Bendahmane, F., Marot, D., Alexis, A., Bendahmane, F., Marot, D., Alexis, A., Parametric, E., Bendahmane, F., Marot, D., and Alexis, A. 2008. Experimental Parametric Study of Suffusion and Backward Erosion. Journal of geotechnical and geoenvironmental engineering, **134**(1): 57–67.

de Boer, R. 2000. Contemporary progress in porous media theory. Applied Mechanics Reviews, **53**(12): 323–70.

Chang, C.S., and Yin, Z.Y. 2011. Micromechanical modeling for behavior of silty sand with influence of fine content. International Journal of Solids and Structures, **48(19)**: 2655–2667.

Chang, D.S. 2012. Internal erosion and overtopping erosion of earth dams and landslide dams.

Chang, D.S., and Zhang, L. 2011. A stress-controlled erosion apparatus for studying internal erosion in soils. Geotechnical Testing Journal, **34**(6): 1–11.

Chang, D.S., and Zhang, L.M. 2013a. Critical Hydraulic Gradients of Internal Erosion under Complex Stress States. Journal of Geotechnical and Geoenvironmental Engineering, **139**(9): 1454–1467.

Chang, D.S., and Zhang, L.M. 2013b. Extended internal stability criteria for soils under seepage. Soils and Foundations, **53(4)**: 569–583.

Chen, C., and Zhang, L. 2021. Hydro-mechanical behaviour of soil experiencing seepage erosion under cyclic hydraulic gradient. Geotechnique,.

Chen, F., Wang, Y., Jiang, W., and Zheng, S. 2021. Numerical simulation of ground movement induced by water and sand gushing in subway through fault based on DEM-CFD. Computers and Geotechnics, **139**: 104282.

Cheng, K., Zhang, C., Peng, K., Liu, H., and Ahmad, M. 2021. Un-resolved CFD-DEM method: An insight into its limitations in the modelling of suffusion in gap-graded soils. Powder Technology, **381**: 520–538.

Cividini, A., Bonomi, S., Vignati, G.C., and Gioda, G. 2009. Seepage-induced erosion in granular soil and consequent settlements. International Journal of Geomechanics, **9**(4): 187–194.

Cundall, P.A., and Strack, O.D.L. 1979. A discrete numerical model for granular

671 assemblies. Geotechnique,.

672 Deng, Z., Wang, G., Jin, W., Tang, N., Ren, H., and Chen, X. 2023. Characteristics
673 and quantification of fine particle loss in internally unstable sandy gravels induced by
674 seepage flow. Engineering Geology, **321**: 107150.

675 Fell, R., and Fry, J.J. 2013. State of The Art on the Likelihood of Internal Erosion
676 of Dams and Levees by Means of Testing. Erosion in Geomechanics Applied to Dams
677 and Levees,: 1–99.

678 Hu, Z., Li, J., Zhang, Y., Yang, Z., and Liu, J. 2023. A CFD-DEM study on the
679 suffusion and shear behaviors of gap-graded soils under stress anisotropy. Acta
680 Geotechnica, **18**(6): 3091–3110.

681 Hu, Z., Zhang, Y., and Yang, Z. 2019. Suffusion-induced deformation and
682 microstructural change of granular soils: a coupled CFD–DEM study. Acta Geotechnica,
683 **14**(3): 795–814.

684 Jin, Y.-F., Yin, Z.-Y., Wu, Z.-X., and Zhou, W.-H. 2018. Identifying parameters of
685 easily crushable sand and application to offshore pile driving. Ocean Engineering, **154**:
686 416–429.

687 Jin, Y.F., Wu, Z.X., Yin, Z.Y., and Shen, J.S. 2017. Estimation of critical state-
688 related formula in advanced constitutive modeling of granular material. Acta
689 Geotechnica, **12**(6): 1329–1351.

690 Ke, L., and Takahashi, A. 2014a. Triaxial erosion test for evaluation of mechanical
691 consequences of internal erosion. Geotechnical Testing Journal, **37**(2).

692 Ke, L., and Takahashi, A. 2014b. Experimental investigations on suffusion
693 characteristics and its mechanical consequences on saturated cohesionless soil. Soils and
694 Foundations, **54**(4): 713–730.

695 Khalil, T., Saiyouri, N., Muresan, B., and Hicher, P. 2013. Internal erosion of
696 chemically reinforced granular materials: a mathematical modeling approach.
697 International journal for numerical and analytical methods in geomechanics, **37**(5): 491–
698 502.

699 Kloss, C., Goniva, C., Hager, A., Amberger, S., and Pirker, S. 2012. Models,
700 algorithms and validation for opensource DEM and CFD-DEM. Progress in
701 Computational Fluid Dynamics, **12**(2–3): 140–152.

702 Liang, Y., Yeh, T.C.J., Wang, J., Liu, M., Zha, Y., and Hao, Y. 2019. Onset of
703 suffusion in upward seepage under isotropic and anisotropic stress conditions. European
704 Journal of Environmental and Civil Engineering, **23**(12): 1520–1534.

705 Liang, Y., Zeng, C., Wang, J.-J., Liu, M.-W., Yeh, T.-C.J., and Zha, Y.-Y. 2017.
706 Constant gradient erosion apparatus for appraisal of piping behavior in upward seepage
707 flow. Geotechnical Testing Journal, **40**(4): 630–642.

708 Liu, Y., Wang, L., Hong, Y., Zhao, J., and Yin, Z.Y. 2020. A coupled CFD-DEM

709 investigation of suffusion of gap graded soil: Coupling effect of confining pressure and
710 fines content. International Journal for Numerical and Analytical Methods in
711 Geomechanics, **44**(18): 2473–2500.

712 Liu, Y., Wang, L., Yin, Z.Y., and Hong, Y. 2023. A coupled CFD-DEM
713 investigation into suffusion of gap-graded soil considering anisotropic stress conditions
714 and flow directions. Acta Geotechnica, **18**(6): 3111–3132.

715 Liu, Y., Yin, Z.Y., Wang, L., and Hong, Y. 2021. A coupled cfd–dem investigation
716 of internal erosion considering suspension flow. Canadian Geotechnical Journal, **58**(9):
717 1411–1425.

718 Marot, D., Le, V.D., Garnier, J., Thorel, L., and Audrain, P. 2012. Study of scale
719 effect in an internal erosion mechanism: Centrifuge model and energy analysis.
720 European Journal of Environmental and Civil Engineering, **16**(1): 1–19.

721 Qian, J.G., Li Weiyi, Yin, Z.Y., and Yang, Y. 2021. Influences of buried depth and
722 grain size distribution on seepage erosion in granular soils around tunnel by coupled
723 CFD-DEM approach. Transportation Geotechnics, **29**: 100574.

724 Reddi, L.N., Lee, I.M., and Bonala, M.V.S. 2000. Comparison of internal and
725 surface erosion using flow pump tests on a sand-kaolinite mixture. Geotechnical testing
726 journal, **23**(1): 116–122.

727 Schaufler, A., Becker, C., and Steeb, H. 2013. Infiltration processes in cohesionless
728 soils. ZAMM-Journal of Applied Mathematics and Mechanics/Zeitschrift für
729 Angewandte Mathematik und Mechanik, **93**(2-3): 138–146.

730 Shire, T., O'Sullivan, C., Hanley, K.J., and Fannin, R.J. 2014. Fabric and Effective
731 Stress Distribution in Internally Unstable Soils. Journal of Geotechnical and
732 Geoenvironmental Engineering,.

733 Steeb, H., Diebels, S., and Vardoulakis, I. 2007. Modeling internal erosion in
734 porous media. *In* Computer Applications In Geotechnical Engineering.

735 Sterpi, D. 2003. Effects of the Erosion and Transport of Fine Particles due to
736 Seepage Flow. International Journal of Geomechanics, **3**(1): 111–122.

737 Taha, H., Nguyen, N.S., Marot, D., Hijazi, A., and Abou-Saleh, K. 2019. Micro-
738 scale investigation of the role of finer grains in the behavior of bidisperse granular
739 materials. Granular Matter, **21**(2): 1–17.

740 Thevanayagam, S., Ravishankar, K., and Mohan, S. 1996. Steady-state strength,
741 relative density, and fines content relationship for sands. Transportation research record,
742 **1547**(1): 61–67.

743 Uzuoka, R., and Borja, R.I. 2012. Dynamics of unsaturated poroelastic solids at
744 finite strain. International Journal for Numerical and Analytical Methods in
745 Geomechanics, **36**(13): 1535–1573.

746 Uzuoka, R., Ichiyama, T., Mori, T., and Kazama, M. 2012. Hydro-mechanical

747 analysis of internal erosion with mass exchange between solid and water. *In* Proceedings
748 of 6th international conference on scour and erosion, Paris.

749 Vardoulakis, I., Stavropoulou, M., and Papanastasiou, P. 1996. Hydro-mechanical
750 aspects of the sand production problem. Transport in porous media, **22**: 225–244.

751 Wan, C.F., and Fell, R. 2008. Assessing the Potential of Internal Instability and
752 Suffusion in Embankment Dams and Their Foundations. Journal of Geotechnical and
753 Geoenvironmental Engineering, **134**(3): 401–407.

754 Wang, P., Ge, Y., Wang, T., Liu, Q., and Song, S. 2022a. CFD-DEM modelling of
755 suffusion in multi-layer soils with different fines contents and impermeable zones.
756 Journal of Zhejiang University-SCIENCE A,: 1–14.

757 Wang, X., Huang, B., Tang, Y., Hu, T., and Ling, D. 2022b. Microscopic
758 mechanism and analytical modeling of seepage-induced erosion in bimodal soils.
759 Computers and Geotechnics, **141**: 104527.

760 Wensrich, C.M., and Katterfeld, A. 2012. Rolling friction as a technique for
761 modelling particle shape in DEM. Powder technology, **217**: 409–417.

762 Wu, Z.-X., Yin, Z.-Y., Jin, Y.-F., and Geng, X.-Y. 2019. A straightforward
763 procedure of parameters determination for sand: a bridge from critical state based
764 constitutive modelling to finite element analysis. European Journal of Environmental
765 and Civil Engineering, **23**(12): 1444–1466.

766 Wu, Z. 2019. Mechanical modelling of sand considering simple shear condition and
767 its application to pile foundation. Phd thesis,.

768 Xie, Z., Wang, S., and Shen, Y. 2023. Roles of clusters in the migration of fines
769 through porous media. Chemical Engineering Science, **265**.

770 Xiong, H., Wu, H., Bao, X., and Fei, J. 2021. Investigating effect of particle shape
771 on suffusion by CFD-DEM modeling. Construction and Building Materials, **289**:
772 123043.

773 Xiong, H., Yin, Z.Y., Zhao, J., and Yang, Y. 2020. Investigating the effect of flow
774 direction on suffusion and its impacts on gap-graded granular soils. Acta Geotechnica,
775 **16(2)**: 399–419.

776 Xiong, H., Zhang, Z., Sun, X., Yin, Z. yu, and Chen, X. 2022. Clogging effect of
777 fines in seepage erosion by using CFD–DEM. Computers and Geotechnics, **152**:
778 105013.

779 Xu, Z.D., Zhang, L.M., Kamali Zarch, M., and Wang, H.J. 2022. Experimental
780 Study of Internal Erosion in Granular Soil Subject to Cyclic Hydraulic Gradient
781 Reversal. Journal of Geotechnical and Geoenvironmental Engineering, **148**(5): 1–11.

782 Yang, J., Yin, Z.Y., Laouafa, F., and Hicher, P.Y. 2019. Modeling coupled erosion
783 and filtration of fine particles in granular media. Acta Geotechnica, **14**(6): 1615–1627.

Yang, J., Yin, Z.Y., Laouafa, F., and Hicher, P.Y. 2020. Hydromechanical modeling of granular soils considering internal erosion. Canadian Geotechnical Journal, **57**(2): 157–172.

Yin, Z.-Y., Wu, Z.-X., and Hicher, P.-Y. 2018. Modeling Monotonic and Cyclic Behavior of Granular Materials by Exponential Constitutive Function. Journal of Engineering Mechanics, **144**(4): 1–13.

Yin, Z.-Y., Yang, J., Laouafa, F., and Hicher, P.-Y. 2020. A framework for coupled hydro-mechanical continuous modelling of gap-graded granular soils subjected to suffusion. European Journal of Environmental and Civil Engineering,: 1–22.

Yin, Z.-Y., Zhao, J., and Hicher, P.-Y. 2014. A micromechanics-based model for sand-silt mixtures. International journal of solids and structures, **51**(6): 1350–1363.

Yin, Z.Y., Huang, H.W., and Hicher, P.Y. 2016. Elastoplastic modeling of sand–silt mixtures. Soils and Foundations,.

Zhao, J., and Shan, T. 2013. Coupled CFD-DEM simulation of fluid-particle interaction in geomechanics. Powder Technology, **239**: 248–258.

Zhou, C., Qian, J., Yin, Z., Liu, Y., and Du, Z. 2023a. Effect of particle shape and bedding angle on suffusion in gap-graded granular soils by coupled CFD-DEM method. **47**(8): 1–26.

Zhou, C., Qian, J., Yin, Z., and Xiong, H. 2023b. Suffusion in gap-graded granular soils subjected to strain-controlled cyclic loading with coupled CFD-DEM method. Transportation Geotechnics, **42**: 101098.

Zhou, C., Qian, J.G., and Yin, Z.Y. 2022. Microscopic investigation of the influence of complex stress states on internal erosion and its impacts on critical hydraulic gradients. International Journal for Numerical and Analytical Methods in Geomechanics, **46**(18): 3377–3401.